

Dependent relevance determination for smooth and structured sparse regression

Anqi Wu

ANQIW@PRINCETON.EDU

*Princeton Neuroscience Institute
Princeton University
Princeton, NJ 08544, USA*

Oluwasanmi Koyejo

SANMI@ILLINOIS.EDU

*Beckman Institute for Advanced Science and Technology
Department of Computer Science
University of Illinois at Urbana-Champaign
Urbana, Illinois, 61801, USA*

Jonathan Pillow

PILLOW@PRINCETON.EDU

*Princeton Neuroscience Institute
Princeton University
Princeton, NJ 08544, USA*

Editor:

Abstract

In many problem settings, parameter vectors are not merely sparse, but dependent in such a way that non-zero coefficients tend to cluster together. We refer to this form of dependency as “region sparsity”. Classical sparse regression methods, such as the lasso and automatic relevance determination (ARD), which model parameters as independent *a priori*, and therefore do not exploit such dependencies. Here we introduce a hierarchical model for smooth, region-sparse weight vectors and tensors in a linear regression setting. Our approach represents a hierarchical extension of the relevance determination framework, where we add a transformed Gaussian process to model the dependencies between the prior variances of regression weights. We combine this with a structured model of the prior variances of Fourier coefficients, which eliminates unnecessary high frequencies. The resulting prior encourages weights to be region-sparse in two different bases simultaneously. We develop Laplace approximation and Monte Carlo Markov Chain (MCMC) sampling to provide efficient inference for the posterior. Furthermore, a two-stage convex relaxation of the Laplace approximation approach is also provided to relax the inevitable non-convexity during the optimization. We finally show substantial improvements over comparable methods for both simulated and real datasets from brain imaging.

Keywords: Bayesian Statistics, Sparsity, Structure Learning, Gaussian Process, fMRI

1. Introduction

Recent work in statistics has focused on high-dimensional inference problems in which the number of parameters equals or exceeds the number of samples. We focus specifically on the linear regression setting: consider a scalar response $y_i \in \mathbb{R}$ generated from an input vector $\mathbf{x}_i \in \mathbb{R}^p$ via the linear model:

$$y_i = \mathbf{x}_i^\top \mathbf{w} + \epsilon_i, \quad \text{for } i = 1, 2, \dots, n, \quad (1)$$

with observation noise $\epsilon_i \sim \mathcal{N}(0, \sigma^2)$. The regression (linear weight) vector $\mathbf{w} \in \mathbb{R}^p$ is the quantity of interest. This general problem is ill-posed when $n \leq p$. However, it is surprisingly tractable when \mathbf{w} has special structure, such as sparsity in an appropriate basis. A large literature has provided theoretical guarantees about the solvability of such problems, as well as a suite of practical methods for solving them.

Methods based on simple sparsity such as the lasso (Tibshirani, 1996) typically treat regression weights as independent *a priori*. This neglects a statistical feature of many real-world problems, which is that non-zero weights tend to arise in local groups or clusters. In many problem settings, weights have an explicit geometric relationship, such as indexing in time (e.g., time series regression) or space (e.g., brain imaging data). If a single regression weight is non-zero, nearby weights in time or space are also likely to be non-zero. Conversely, in a region where most weights are zero, any particular coefficient is also likely to be zero. Thus, nearby weights exhibit dependencies that are not captured by independent priors. We refer to this form of dependency as *region sparsity*.

A variety of methods have been developed to incorporate local dependencies between regression weights, such as the group lasso (Yuan and Lin, 2006). However, these methods typically require the user to pre-specify the group size or to partition the weights into groups *a priori*. Such information is unavailable in many applications of interest, and hard partitioning into groups breaks dependencies between nearby coefficients that are assigned to different groups.

In this paper, we take a Bayesian approach to inferring regression weights with region-sparse structure. We introduce a hierarchical prior over \mathbf{w} of the form:

$$\mathbf{u} \sim \mathcal{GP} \quad (2)$$

$$\mathbf{w}|\mathbf{u} \sim \mathcal{N}(0, C(\mathbf{u})), \quad (3)$$

where \mathbf{u} is a latent vector that captures dependencies in the sparsity pattern of \mathbf{w} , and $\mathbf{w}|\mathbf{u}$ has a zero-mean Gaussian distribution with a diagonal covariance matrix $C(\mathbf{u})$, given by a deterministic function of \mathbf{u} . We use a Gaussian process (GP) prior over \mathbf{u} to encode structural assumptions about region sparsity (e.g., the typical size of clusters of non-zero weights and the spacing between them). This model can be seen as an extension of automatic relevance determination (ARD), in which the elements of \mathbf{u} are *a priori* independent (Neal, 1995; MacKay, 1992). We therefore refer to it as *dependent relevance determination* (DRD).

Note that region-sparsity refers only to the sparsity pattern of regression weights, i.e., the locations where they are non-zero, not to the particular values of the weights themselves.

This is reflected in the fact that we define the DRD prior covariance matrix $C(\mathbf{u})$ to be diagonal, making the weights conditionally independent given the pattern defined by \mathbf{u} . In many cases, however, we expect weights to be smooth as well as sparse due to continuity of the input regressors in space or time. Most of the real data do exhibit spatial and temporal correlations. Coefficients usually possess contiguous regions and smoothness. Hence, we are aiming at developing a universal approach easily integrating both structured sparsity and smoothness concurrently. To incorporate smoothness, we combine the standard DRD prior with a squared exponential covariance function. The resulting prior has a non-diagonal covariance matrix that encourages smoothness as well as sparsity. We refer to this extension as *smooth dependent relevance determination* (smooth-DRD). Samples from the smooth-DRD prior have local islands of smooth and non-zero weights, surrounded by large regions of zeros. We will show that combining region-sparsity and smoothness together will significantly enhance the performance in a non-trivial way.

Unfortunately, exact inference under DRD and smooth-DRD priors is analytically intractable. We therefore introduce a fast approximate inference method based on a Laplace approximation to the posterior over \mathbf{u} , and a sampling-based inference method using Monte Carlo Markov Chain (MCMC) sampling. We also derive a two-stage convex relaxation of the Laplace approximation approach in order to overcome the effects of bad local optima.

We show experimental evaluations on 1D simulated datasets comparing the performance among different methods. In addition, the phase transition curve analyses are carried out against lasso to show the superiority of DRD and smooth-DRD in support recovery for group structure sparsity with or without smoothness. Furthermore, the DRD based priors are exploited for three neuroimaging datasets. Domain expertise and current evidence in neuroimaging suggest that discrimination performance is primarily driven by spatially smooth activation within spatially sparse regions, and several estimation algorithms have been proposed that exploit this structure (Michel et al., 2011; Baldassarre et al., 2012; Gramfort et al., 2013; Grosenick et al., 2011). We provide experimental comparisons to these methods, showing the superiority of DRD in practice. It's shown to yield more interpretable weight maps and improved discriminative quantities is well established finally.

Here we highlight our key contributions as follows:

- We introduce a new hierarchical model for smooth, region-sparse weight tensors. The model uses a Gaussian process to introduce dependencies between prior variances of regression weights governing localized sparsity in weights and simultaneously imposes smoothness by integrating a smoothness-inducing covariance function into the prior distribution of weights.
- We describe two methods for inferring the model parameters: one based on the Laplace approximation and a second based on MCMC. We propose a fast approximate inference method based on the Laplace approximation involving a novel two-stage convex relaxation of the log posterior in order to overcome the effects of bad local optima.
- We show phase transition curves governing the transition from imperfect to near-perfect recovery for lasso and DRD estimators, revealing that group structure and smoothness can have a major impact on the recoverability of sparse signals.

This paper is organized as follows. In Sec. 2, we review the related structured sparsity literature. In Sec. 3, we introduce our new region-sparsity and smoothness inducing priors. In Sec. 4, we propose two approaches to Bayesian inference for the parameter estimation, the evidence optimization via Laplace approximation and the MCMC sampling. A two-stage convex relaxation of the Laplace approximation approach is also introduced to alleviate the non-convexity with a more robust two-stage convexity. Sec. 5 introduces a detailed analysis of the structured sparsity and smoothness properties of the DRD based priors and the other methods that can be used for this purpose. Sec. 6 presents the phase transition analysis for lasso and DRD estimators. Sec. 7 shows some experiments on three real fMRI datasets, comparing the different methods that can be used for structured sparsity. Finally, Sec. 8 presents the conclusion and discussion of this work.

2. Related work

The classic method for sparse variable selection is the lasso, introduced by Tibshirani (1996), which places an l_1 penalty on the regression weights. This method can be interpreted as a *maximum a posteriori* (MAP) estimate under a Laplace (or double-exponential) prior. A fully Bayesian treatment of this model was later developed by Park and Casella (2008). A variety of Bayesian methods based on other sparsity-inducing prior distributions have been developed, including the horseshoe prior (Carvalho et al., 2009), which uses a continuous density with an infinitely tall spike at the origin and heavy tails, and the spike-and-slab prior (Mitchell and Beauchamp, 1988) which consists of a weighted mixture of mixture of a delta function (the spike) and a broad Gaussian (the slab), both centered at the origin.

Another approach to sparse variable selection comes from empirical Bayes (also known as evidence optimization or “type-II” marginal likelihood). These methods rely on a two-step inference procedure: (1) optimize hyperparameters governing the sparsity pattern via ascent of the marginal likelihood; and then (2) compute MAP estimates of the parameters given the hyperparameters. The most popular such estimator is automatic relevance determination (ARD), which prunes unnecessary coefficients by optimizing precision of each regression coefficient under a Gaussian model (Neal, 1995; MacKay, 1992). The relevance vector machine (RVM) was later formulated as a general Bayesian framework for obtaining sparse solutions to regression and classification tasks (Tipping, 2001). The RVM has an identical functional form to the support vector machine, but provides probabilistic analysis. Tipping and Faul (2003) then was proposed for RVM to scale up to large scale training procedure.

All these methods can be interpreted as imposing a sparse and independent prior on the regression weights. The resulting posterior over weights has high concentration near the axes, so that many weights end up at zero unless forced away strongly by the likelihood.

In the field of the structured sparsity learning, group lasso is the most straightforward extension of lasso to capture sparsity existing across collections of variables (Yuan and Lin, 2006). They achieved the group sparse structure by introducing an l_1 penalty on the l_2 norms of each group. Moreover, Huang et al. (2011) generalized the group sparsity idea by using coding complexity regularization methods associated with the structure. A variety of other papers have proposed alternative approaches to correlated or structured regularization

(Jacob et al., 2009; Liu et al., 2009; Kim and Xing, 2009; Friedman et al., 2010; Jenatton et al., 2011).

Previous literature has also explored Bayesian methods for structured sparse inference. A common strategy is to introduce a latent multivariate Gaussian that controls the correlation structure governing conditionally independent densities over coefficients. Gerven et al. (2009) extended the univariate Laplace prior to a novel multivariate Laplace distribution represented as a scale mixture that induces coupling. Hernández-Lobato and Hernández-Lobato (2013) described a similar approach that results in a marginally horseshoe prior. Several other papers have proposed dependent generalizations of the spike-and-slab prior. Hernández-Lobato et al. (2013) described a group spike-and-slab distribution using a multivariate Bernoulli distribution over the indicators of the spikes associated with a group specification. Subsequently, Andersen et al. (2014, 2015) relaxed the hard-coded group specification by encoding the structure with a generic covariance function. Meanwhile, Engelhardt and Adams (2014) introduced a Bayesian model for structured sparsity that uses a Gaussian process (GP) to control mixing weights of the spike and slab prior in proportion to feature similarity. Apart from imposing the correlation structure on the independent spike and slab elements, Yu et al. (2012) put forward a hierarchical Bayesian framework with the mixing weights of the cluster patterns generated from Beta distributions. Our work is most similar to Engelhardt and Adams (2014) and Andersen et al. (2015), except that we use an ARD-like approach with a conditionally Gaussian density over coefficients instead of a spike and slab prior. Our work is also the first that we are aware of that simultaneously captures sparsity and smoothness.

3. Dependent relevance determination (DRD) priors

In this section, we introduce the DRD prior and the smooth-DRD prior, an extension to incorporate smoothness of regression weights. We focus on the linear regression setting with conditional responses distributed as:

$$\mathbf{y}|X, \mathbf{w}, \sigma^2 \sim \mathcal{N}(\mathbf{y}|X\mathbf{w}, \sigma^2 I), \quad (4)$$

where $X = [\mathbf{x}_1, \dots, \mathbf{x}_n]^\top \in \mathbb{R}^{n \times p}$ denotes the design matrix, $\mathbf{y} = [y_1, \dots, y_n]^\top \in \mathbb{R}^n$ is the observation vector, and σ^2 is the observation noise variance, where p is the dimension of the input vectors and n is the number of samples.

3.1 Automatic relevance determination

The relevance determination framework includes a family of estimators that rely on a zero-mean multivariate normal prior:

$$\mathbf{w}|\boldsymbol{\theta} \sim \mathcal{N}(0, C(\boldsymbol{\theta})), \quad (5)$$

where the prior covariance matrix $C(\boldsymbol{\theta})$ is a function of some hyperparameters $\boldsymbol{\theta}$. The form of the dependence of C on $\boldsymbol{\theta}$ leads to different forms of assumed structure, including sparsity

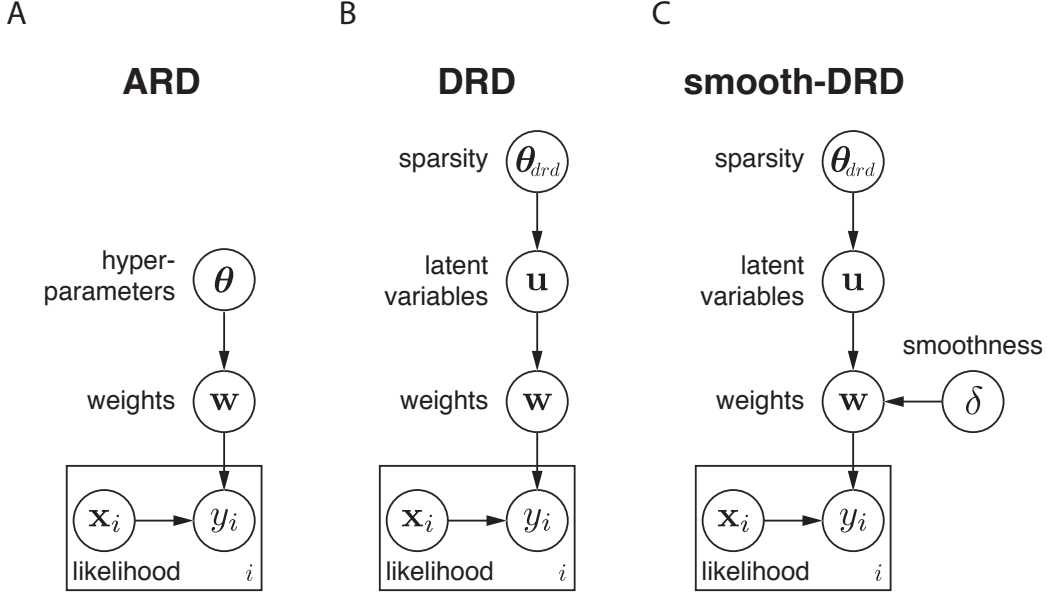


Figure 1: Graphical models for ARD, DRD and smooth-DRD.

(Tipping, 2001; Tipping and Faul, 2002; Wipf and Nagarajan, 2008), smoothness (Sahani and Linden, 2003; Schmolck, 2008), or locality (Park and Pillow, 2011).

Automatic relevance determination (ARD) defines the prior covariance to be diagonal, $C_{ii} = \theta_i^{-1}$, where a distinct hyperparameter θ_i specifies the prior precision for the i 'th regression coefficient. ARD places an independent improper gamma prior on each hyperparameter, $\theta_i \sim \text{gamma}(0, 0)$, and performs inference for $\{\theta_i\}$ by maximizing marginal likelihood. This sends many θ_i to infinity, pruning the corresponding coefficients out of the model. A typical graphical model for ARD is presented in Fig. 1A. The independence assumption in the prior over hyperparameters means that there is no tendency for nearby coefficients to remain in or be pruned from the model. This is the primary shortcoming that our method seeks to overcome.

3.2 DRD: A hierarchical extension of ARD

We extend the standard ARD model by adding a level of hierarchy. Instead of directly optimizing hyperparameters that control sparsity of each weight, as in ARD, we introduce a latent vector governed by a GP prior to capture dependencies in the sparsity pattern over weights (see Fig. 1B). Let $\mathbf{u} \in \mathbb{R}^p$ denote a latent vector distributed according to a GP prior

$$\mathbf{u} \sim \mathcal{GP}(\mathbf{b}\mathbf{1}, K), \quad (6)$$

where $b \in \mathbb{R}$ is the scalar mean, $\mathbf{1}$ is a length- p vector of ones, and covariance matrix K is determined by a squared exponential kernel. The i, j 'th entry of K is given by

$$K_{ij} = \rho \exp\left(-\frac{\|\chi_i - \chi_j\|^2}{2l^2}\right), \quad (7)$$

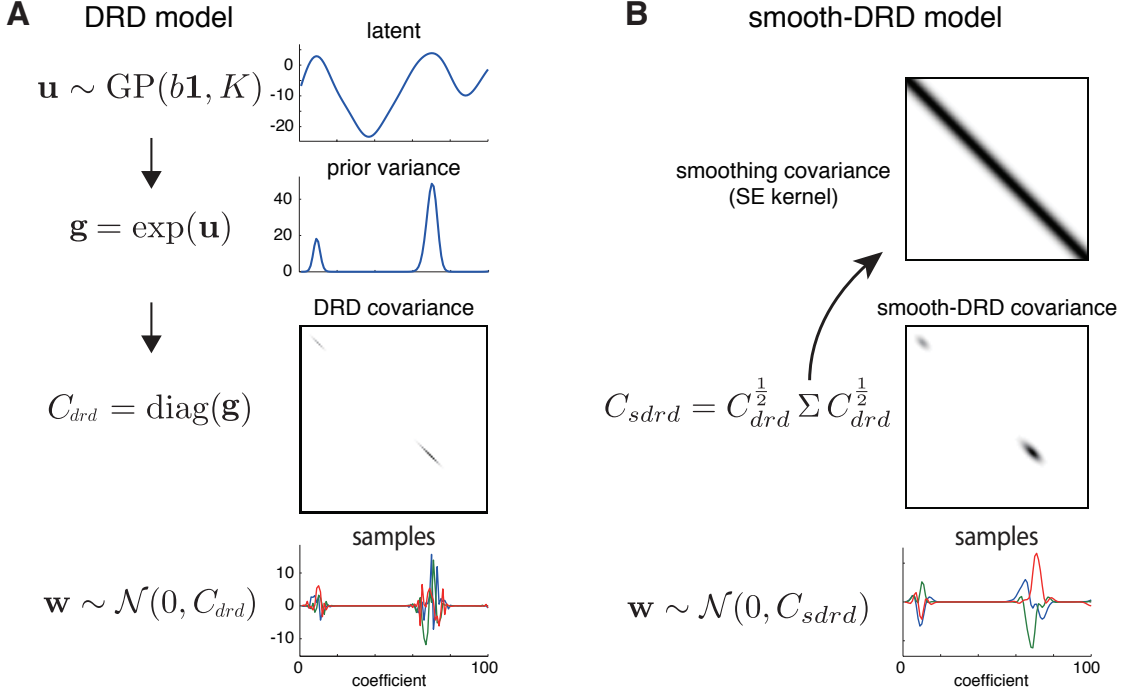


Figure 2: The sampling procedures for the generative models of DRD and smooth-DRD.

where χ_i and χ_j are the spatial locations of weights w_i and w_j , respectively, and kernel hyperparameters are the marginal variance $\rho > 0$ and length scale $l > 0$. Samples from this GP on a grid of locations $\{\chi_i\}$ are smooth on the scale of l , and have mean b and marginal variance ρ .

To obtain a prior over region-sparse weight vectors, we transform \mathbf{u} to the positive reals via a nonlinear function f , and the transformed latent vector $\mathbf{g} = f(\mathbf{u})$ forms the diagonal of a diagonal covariance matrix for a zero-mean Gaussian prior over the weights:

$$C_{drd} = \text{diag}[f(\mathbf{u})], \quad (8)$$

where f is a monotonically increasing function that squashes negative values of \mathbf{u} to near zero. Here we will mainly consider the exponential function $f(u) = \exp(u)$, but we will also consider “soft-rectification” function $f(u) = \log(1 + \exp(u))$ in the experiment for numerical stability. When the GP mean b is very negative relative to the prior standard deviation $\sqrt{\rho}$, most elements of \mathbf{g} will be close to zero, resulting in weights \mathbf{w} with a high degree of sparsity (i.e., few weights far from zero). The length scale l determines the smoothness of samples \mathbf{u} and thereby determines the typical width of bumps in the prior variance \mathbf{g} . We denote the set of hyperparameters governing the GP prior on \mathbf{u} by $\boldsymbol{\theta}_{drd} = \{b, \rho, l\}$. Fig. 2A shows a depiction of sampling from the DRD generative model.

3.3 Smooth-DRD

The standard DRD model imposes smooth dependencies in the prior variances of the regression weights, but the weights themselves remain uncorrelated (as reflected by the fact that the covariance C_{drd} is diagonal). In many settings, however, we expect weights to exhibit smoothness in addition to region sparsity. To capture this property, we can augment DRD with a second Gaussian process, denoted as smooth-DRD, that induces smoothness, contributing off-diagonal structure to the prior covariance matrix while preserving the marginal variance pattern imposed by DRD (see Fig. 1C).

Let Σ denote a covariance matrix governed by a standard squared-exponential GP kernel:

$$\Sigma_{ij} = \exp\left(-\frac{\|\chi_i - \chi_j\|^2}{2\delta^2}\right), \quad (9)$$

with length scale δ and marginal variance set to 1. Then we define the *smooth-DRD* covariance as the “sandwich” matrix given by:

$$C_{smooth-DRD} = C_{drd}^{\frac{1}{2}} \Sigma C_{drd}^{\frac{1}{2}}, \quad (10)$$

where $C_{drd}^{\frac{1}{2}}$ is simply the matrix square root of the diagonal covariance matrix C_{drd} . The resulting matrix has the same diagonal entries as C_{drd} , but has off-diagonal structure governed by Σ that induces smoothness. This matrix is obviously positive semi-definite because, for all $\mathbf{x} \in \mathbb{R}^p$, $\mathbf{x}^\top C_{smooth-DRD} \mathbf{x} = (C_{drd}^{\frac{1}{2}} \mathbf{x})^\top \Sigma (C_{drd}^{\frac{1}{2}} \mathbf{x}) \geq 0$, due to the positive semi-definiteness of Σ . It is therefore a valid covariance matrix. Fig. 2B shows a depiction of sampling from the smooth-DRD generative model. In the following, we will let $\boldsymbol{\theta}$ denote the entire hyperparameter set for smooth-DRD prior and the noise variance, where $\boldsymbol{\theta} = \{\boldsymbol{\theta}_{drd}, \delta, \sigma^2\}$.

4. Parameter estimation

In this section, we describe two methods for inference under the DRD and smooth-DRD priors: (1) empirical Bayesian inference via evidence optimization using the Laplace approximation; and (2) fully Bayesian inference via MCMC sampling. The first seeks to find the MAP estimate of the latent vector \mathbf{u} governing region sparsity via optimization of the log marginal likelihood, and then provides a conditional MAP estimate of the weights \mathbf{w} . The second uses MCMC sampling to integrate over \mathbf{u} and provides the posterior mean of \mathbf{w} given the data via an average over samples.

4.1 Empirical Bayes inference with Laplace approximation

The likelihood $p(\mathbf{y}|X, \mathbf{w}, \sigma^2)$ (eq. 4) and the prior $p(\mathbf{w}|\mathbf{u}, \boldsymbol{\theta}_{drd}, \delta)$ (eq. 5) are both Gaussian given the latent variables \mathbf{u} and hyperparameters $\boldsymbol{\theta}$, giving a conditionally Gaussian posterior over the regression weights:

$$p(\mathbf{w}|X, \mathbf{y}, \mathbf{u}, \boldsymbol{\theta}) = \mathcal{N}(\boldsymbol{\mu}_{\mathbf{w}}, \Lambda_{\mathbf{w}}), \quad (11)$$

with covariance and mean given by

$$\Lambda_{\mathbf{w}} = (\frac{1}{\sigma^2} X^\top X + C^{-1})^{-1}, \quad \boldsymbol{\mu}_{\mathbf{w}} = \frac{1}{\sigma^2} \Lambda_{\mathbf{w}} X^\top \mathbf{y}, \quad (12)$$

where prior covariance matrix C is a function of \mathbf{u} and $\boldsymbol{\theta}$. The posterior mean $\boldsymbol{\mu}_{\mathbf{w}}$ is also the MAP estimate of \mathbf{w} given latent vector \mathbf{u} and hyperparameters $\boldsymbol{\theta}$.

Empirical Bayes inference involves setting the hyperparameters by maximizing the marginal likelihood or evidence, given by

$$p(\mathbf{y}|X, \boldsymbol{\theta}) = \iint p(\mathbf{y}|X, \mathbf{w}, \sigma^2) p(\mathbf{w}|\mathbf{u}, \delta) p(\mathbf{u}|\boldsymbol{\theta}_{drd}) d\mathbf{w} d\mathbf{u}. \quad (13)$$

We can take the integral over \mathbf{w} analytically due to the conditionally Gaussian prior and the likelihood, giving the simplified expression

$$p(\mathbf{y}|X, \boldsymbol{\theta}) = \int p(\mathbf{y}|X, \mathbf{u}, \sigma^2, \delta) p(\mathbf{u}|\boldsymbol{\theta}_{drd}) d\mathbf{u}, \quad (14)$$

where the conditional evidence given \mathbf{u} is a normal density evaluated at \mathbf{y} ,

$$p(\mathbf{y}|X, \mathbf{u}, \boldsymbol{\theta}) = \mathcal{N}(\mathbf{y}|\mathbf{0}, X C X^\top + \sigma^2 I). \quad (15)$$

However, the integral over \mathbf{u} has no analytic form. We therefore resort to the Laplace's method to approximate this integral.

4.1.1 LAPLACE APPROXIMATION

Laplace's method provides a technique for approximating intractable integrals using a second-order Taylor expansion in \mathbf{u} of log of the integrand in (eq. 14). This method is equivalent to approximating the posterior over \mathbf{u} given $\boldsymbol{\theta}$ by a Gaussian centered on its mode (MacKay (2003), chap. 27). The exact posterior is given by Bayes' rule:

$$p(\mathbf{u}|X, \mathbf{y}, \boldsymbol{\theta}) = \frac{1}{Z} p(\mathbf{y}|X, \mathbf{u}, \sigma^2, \delta) p(\mathbf{u}|\boldsymbol{\theta}_{drd}), \quad (16)$$

where the normalizing constant, $Z = p(\mathbf{y}|X, \boldsymbol{\theta})$, is the marginal likelihood we wish to compute. The Gaussian approximation to the posterior is

$$p(\mathbf{u}|X, \mathbf{y}, \boldsymbol{\theta}) \approx \mathcal{N}(\mathbf{m}_{\mathbf{u}}, \Lambda_{\mathbf{u}}), \quad (17)$$

where $\mathbf{m}_{\mathbf{u}}$ is the posterior mode and $\Lambda_{\mathbf{u}}$ is a local approximation to the posterior covariance. Substituting this approximation into (eq. 16), we can directly solve for Z :

$$Z \approx \frac{p(\mathbf{y}|X, \mathbf{u}, \sigma^2, \delta) p(\mathbf{u}|\boldsymbol{\theta}_{drd})}{\mathcal{N}(\mathbf{m}_{\mathbf{u}}, \Lambda_{\mathbf{u}})}. \quad (18)$$

The right-hand-side of this expression can be evaluated at any \mathbf{u} , but it is conventional to use the mode, $\mathbf{u} = \mathbf{m}_{\mathbf{u}}$, given that this is where the approximation is most accurate.

To compute the Laplace approximation, we first numerically optimize the log of the posterior (eq. 16) to find its mode:

$$\mathbf{m}_{\mathbf{u}} = \arg \max_{\mathbf{u}} \left[\log p(\mathbf{y}|X, \mathbf{u}, \sigma^2, \delta) + \log p(\mathbf{u}|\boldsymbol{\theta}_{drd}) \right], \quad (19)$$

where the first term is the log of the conditional evidence given \mathbf{u} (eq. 15),

$$\log p(\mathbf{y}|X, \mathbf{u}, \sigma^2, \delta) = -\frac{1}{2} \log |XCX^\top + \sigma^2 I| - \frac{1}{2} \mathbf{y}^\top (XCX^\top + \sigma^2 I)^{-1} \mathbf{y} + \text{const}, \quad (20)$$

and the second is the log of the GP prior for \mathbf{u} ,

$$\log p(\mathbf{u}|\boldsymbol{\theta}_{drd}) = -\frac{1}{2} (\mathbf{u} - b\mathbf{1})^\top K^{-1} (\mathbf{u} - b\mathbf{1}) - \frac{1}{2} \log |K| + \text{const}. \quad (21)$$

We use quasi-Newton methods to optimize this objective function because the fixed point methods developed for ARD (e.g., MacKay (1992); Tipping and Faul (2003)), which operate on one element of the prior precision vector at a time, are inefficient due to the strong dependencies induced by the GP prior. However, because this high-dimensional optimization problem is non-convex, we also formulate a novel approach for optimizing \mathbf{u} using a two-stage convex relaxation inspired by Wipf and Nagarajan (2008) (Sec. 4.1.2).

Given the mode of the log-posterior $\mathbf{m}_{\mathbf{u}}$, the second step to computing the Laplace-based approximation to the marginal likelihood is to compute the Hessian (2nd derivative matrix) of the log-posterior at $\mathbf{m}_{\mathbf{u}}$. The negative inverse of the Hessian gives us the posterior covariance for the Laplace approximation (eq. 17):

$$\Lambda_{\mathbf{u}} = \left(-\frac{\partial^2}{\partial \mathbf{u} \partial \mathbf{u}^\top} \left[\log p(\mathbf{y}|X, \mathbf{u}, \sigma^2, \delta) + \log p(\mathbf{u}|\boldsymbol{\theta}_{drd}) \right] \right)^{-1}. \quad (22)$$

See the Appendix A for the explicit derivation of Hessian for the DRD model.

Given these ingredients, we can now write down the approximation to the log marginal likelihood (eq. 18):

$$\log p(\mathbf{y}|X, \boldsymbol{\theta}) \approx \log p(\mathbf{y}|X, \mathbf{m}_{\mathbf{u}}, \sigma^2, \delta) + \log p(\mathbf{m}_{\mathbf{u}}|\boldsymbol{\theta}_{drd}) + \frac{1}{2} \log |\Lambda_{\mathbf{u}}| + \text{const}, \quad (23)$$

where the first term is simply the log conditional evidence (eq. 20) with prior covariance C evaluated at $\mathbf{m}_{\mathbf{u}}$.

It is this log-marginal likelihood that we seek to optimize in order to learn hyperparameters $\boldsymbol{\theta}$. The key difficulty is that the Laplace approximation parameters $\mathbf{m}_{\mathbf{u}}$ and $\Lambda_{\mathbf{u}}$ depend implicitly on $\boldsymbol{\theta}$ (since $\mathbf{m}_{\mathbf{u}}$ is determined by numerical optimization at a fixed value of $\boldsymbol{\theta}$), making it impractical to evaluate their derivatives with respect to $\boldsymbol{\theta}$. To address this problem, we introduce a method for partially decoupling the Laplace approximation from the hyperparameters (Sec. 4.1.3).

4.1.2 A TWO-STAGE CONVEX RELAXATION TO LAPLACE APPROXIMATION

The optimization for $\mathbf{m}_{\mathbf{u}}$ (eq. 19), the mode of the posterior over the latent vector \mathbf{u} , is a critical step for computing the Laplace approximation. However, the negative log-posterior

is a non-convex function in \mathbf{u} , meaning that there is no guarantee of obtaining the global minimum. In this, DRD resembles the original ARD model. Neither of the two most popular optimization methods for ARD, MacKay's fixed-point method (MacKay, 1992) and Tipping and Faul's fast-ARD (Tipping and Faul, 2003), are guaranteed to converge to a local minimum or even a fixed point of the log-posterior.

In this section, we introduce an alternative formulation of the cost function in (eq. 19) using an auxiliary function: this provides a tight convex upper bound that can be optimized more easily. The technique is similar to the iterative re-weighted l_1 formulation of ARD in Wipf and Nagarajan (2008).

Let $\mathcal{L}(\mathbf{u})$ denote the sum of terms in the negative log-posterior (eq. 19) that involve \mathbf{u} ,

$$\mathcal{L}(\mathbf{u}) = \frac{1}{2} \log |XCX^\top + \sigma^2 I| + \frac{1}{2} \mathbf{y}^\top (XCX^\top + \sigma^2 I)^{-1} \mathbf{y} + \frac{1}{2} (\mathbf{u} - b\mathbf{1})^\top K^{-1} (\mathbf{u} - b\mathbf{1}), \quad (24)$$

where $C = \text{diag}(e^{\mathbf{u}})$. We denote the three terms it contains as:

$$\mathcal{L}_1(\mathbf{u}) = \frac{1}{2} \log |X \text{diag}(e^{\mathbf{u}}) X^\top + \sigma^2 I| \quad (25)$$

$$\mathcal{L}_2(\mathbf{u}) = \frac{1}{2} \mathbf{y}^\top (X \text{diag}(e^{\mathbf{u}}) X^\top + \sigma^2 I)^{-1} \mathbf{y} \quad (26)$$

$$\mathcal{L}_3(\mathbf{u}) = \frac{1}{2} (\mathbf{u} - b\mathbf{1})^\top K^{-1} (\mathbf{u} - b\mathbf{1}). \quad (27)$$

Here $\mathcal{L}_1(\mathbf{u})$ and $\mathcal{L}_3(\mathbf{u})$ are both convex in \mathbf{u} (see proof in Appendix B). We can derive a tight convex upper bound for $\mathcal{L}_2(\mathbf{u})$, thus providing a tight convex upper bound for $\mathcal{L}(\mathbf{u})$.

We know that $\mathcal{L}_2(\mathbf{u})$ is non-convex, but we are interested in rewriting it using concave duality. Let $\mathbf{h}(\mathbf{u}) : \mathbb{R}^p \rightarrow \Omega \subset \mathbb{R}^p$ be a mapping with range Ω , which may or may not be a one-to-one map. We assume that there exists a function $\bar{\mathcal{L}}_{\mathbf{h}}(\boldsymbol{\eta})$ defined on Ω such that $\mathcal{L}_2(\mathbf{u}) = \bar{\mathcal{L}}_{\mathbf{h}}(\mathbf{h}(\mathbf{u}))$ holds. We assume that we can find \mathbf{h} so that the function $\bar{\mathcal{L}}_{\mathbf{h}}(\boldsymbol{\eta})$ is a concave function of $\boldsymbol{\eta}$ on Ω . To exploit this technique, we first rewrite \mathcal{L}_2 using the matrix inverse lemma (Higham, 2002) as:

$$\mathcal{L}_2(\mathbf{u}) = \frac{1}{2\sigma^2} \mathbf{y}^\top \mathbf{y} - \frac{1}{2\sigma^4} \mathbf{y}^\top X \left(\frac{1}{\sigma^2} X^\top X + \text{diag}(e^{-\mathbf{u}}) \right)^{-1} X^\top \mathbf{y}. \quad (28)$$

Then, setting $\mathbf{h}(\mathbf{u}) = e^{-\mathbf{u}}$, which is convex in \mathbf{u} , we have

$$\bar{\mathcal{L}}_{\mathbf{h}}(\mathbf{h}(\mathbf{u})) = \frac{1}{2\sigma^2} \mathbf{y}^\top \mathbf{y} - \frac{1}{2\sigma^4} \mathbf{y}^\top X \left(\frac{1}{\sigma^2} X^\top X + \text{diag}(\mathbf{h}(\mathbf{u})) \right)^{-1} X^\top \mathbf{y}. \quad (29)$$

This expression is concave in $\boldsymbol{\eta} = \mathbf{h}(\mathbf{u})$ (see Section 3.1.5 of Boyd and Vandenberghe (2004)), and thus can be expressed as a minimum over upper-bounding hyperplanes via

$$\mathcal{L}_2(\mathbf{u}) = \bar{\mathcal{L}}_{\mathbf{h}}(\mathbf{h}(\mathbf{u})) = \inf_{\mathbf{z} \in \mathbb{R}^p} \left[\mathbf{z}^\top \mathbf{h}(\mathbf{u}) - \mathcal{L}_{\mathbf{h}}^*(\mathbf{z}) \right], \quad (30)$$

where $\mathcal{L}_{\mathbf{h}}^*(\mathbf{z})$ is the concave conjugate of $\bar{\mathcal{L}}_{\mathbf{h}}(\boldsymbol{\eta})$ that is defined by the duality relationship

$$\mathcal{L}_{\mathbf{h}}^*(\mathbf{z}) = \inf_{\boldsymbol{\eta} \in \mathbb{R}^p} \left[\mathbf{z}^\top \boldsymbol{\eta} - \bar{\mathcal{L}}_{\mathbf{h}}(\boldsymbol{\eta}) \right], \quad (31)$$

Algorithm 1 A two-stage convex relaxation method for DRD Laplace approximation

Input: $X, \mathbf{y}, \boldsymbol{\theta}$ **Output:** $\hat{\mathbf{u}}$ initialize dual variable $\hat{\mathbf{z}}_i = 1, \forall i = 1, 2, \dots, p$

Repeat the following two steps until convergence:

1. Fix $\hat{\mathbf{z}}$, let $\hat{\mathbf{u}} = \operatorname{argmin}_{\mathbf{u} \in \mathbb{R}^p} [\mathbf{z}^\top \mathbf{h}(\mathbf{u}) + \mathcal{L}_1(\mathbf{u}) + \mathcal{L}_3(\mathbf{u})]$ in (eq. 33)
 2. Fix $\hat{\mathbf{u}}$, let $\hat{\mathbf{z}} = \nabla_{\boldsymbol{\eta}} \bar{\mathcal{L}}_{\mathbf{h}}(\boldsymbol{\eta})|_{\boldsymbol{\eta}=\mathbf{h}(\hat{\mathbf{u}})}$ in (eq. 34)
-

and \mathbf{z} is the dual variable. Note, however, that for our purpose it is not necessary to ever explicitly compute $\mathcal{L}_{\mathbf{h}}^*(\mathbf{z})$. This leads to the following upper-bounding auxiliary cost function

$$\bar{\mathcal{L}}_{\mathbf{h}}(\boldsymbol{\eta}, \mathbf{z}) = \mathbf{z}^\top \boldsymbol{\eta} - \mathcal{L}_{\mathbf{h}}^*(\mathbf{z}) \geq \bar{\mathcal{L}}_{\mathbf{h}}(\boldsymbol{\eta}). \quad (32)$$

Thus, it naturally admits the tight convex upper bound for $\mathcal{L}(\mathbf{u})$,

$$\mathcal{L}(\mathbf{u}, \mathbf{z}) \triangleq \mathbf{z}^\top \mathbf{h}(\mathbf{u}) - \mathcal{L}_{\mathbf{h}}^*(\mathbf{z}) + \mathcal{L}_1(\mathbf{u}) + \mathcal{L}_3(\mathbf{u}) \geq \mathcal{L}(\mathbf{u}). \quad (33)$$

Moreover, for any fixed $\boldsymbol{\eta} = \mathbf{h}(\mathbf{u})$, it's well-known that the minimum of the right hand side of (eq. 31) is achieved at

$$\hat{\mathbf{z}} = \nabla_{\boldsymbol{\eta}} \bar{\mathcal{L}}_{\mathbf{h}}(\boldsymbol{\eta})|_{\boldsymbol{\eta}=\mathbf{h}(\mathbf{u})}. \quad (34)$$

This leads to the general optimization procedure presented in Algorithm 1. By repeatedly refining the dual parameter \mathbf{z} , we can obtain a repeatedly improved convex relaxation, leading to a solution superior to that of the initial convex relaxation.

Now we show the analysis of global convergence. According to the Zangwill's *Global Convergence Theorem* (Zangwill, 1969), let $\mathcal{A}(\cdot) : \mathcal{U} \rightarrow \mathcal{P}(\mathcal{U})$ be a point-to-set mapping to handle the multi-global minima case, which satisfies Steps 1 and 2 of the proposed algorithm, then

Theorem 1 *From any initialization point $\mathbf{u}^0 \in \mathbb{R}^p$, the sequence of parameter estimates $\{\mathbf{u}^k\}$ generated via $\mathbf{u}^{k+1} \in \mathcal{A}(\mathbf{u}^k)$ is guaranteed to converge monotonically to a local minimum (or saddle point) of $\mathcal{L}(\mathbf{u})$.*

Proof Let $\Gamma \in \mathcal{U}$ be a solution set. In order to use the global convergence theorem, we need to show that

- 1) all points $\{\mathbf{u}^k\}$ are contained in a compact set $S \in \mathcal{U}$, where \mathcal{U} is \mathbb{R}^p in our problem;
- 2) there is a continuous function Z on \mathcal{U} such that
 - (a) if $x \notin \Gamma$, then $Z(y) < Z(x)$ for all $y \in \mathcal{A}(x)$;
 - (b) if $x \in \Gamma$, then $Z(y) \leq Z(x)$ for all $y \in \mathcal{A}(x)$;
- 3) the mapping \mathcal{A} is closed at points outside Γ .

First, let's define the mapping \mathcal{A} to be achieved by

$$\mathbf{u}^{k+1} = \operatorname{argmin}_{\mathbf{u} \in \mathbb{R}^p} \mathcal{F}(\mathbf{u}) = \operatorname{argmin}_{\mathbf{u} \in \mathbb{R}^p} \mathbf{z}^{k\top} \mathbf{h}(\mathbf{u}) - \mathcal{L}_{\mathbf{h}}^*(\mathbf{z}) + \mathcal{L}_1(\mathbf{u}) + \mathcal{L}_3(\mathbf{u}) \quad (35)$$

where $\mathbf{z}^k = \nabla_{\boldsymbol{\eta}} \tilde{\mathcal{L}}_{\mathbf{h}}(\boldsymbol{\eta})|_{\boldsymbol{\eta}=\mathbf{h}(\mathbf{u}^k)}$. We can prove that when $\|\mathbf{u}\| \rightarrow \infty$, we have $\mathcal{F}(\mathbf{u}) \rightarrow \infty$ (proof in Appendix C). Therefore, the solution set of $\mathcal{F}(\mathbf{u})$ is bounded and nonempty. Accordingly, $\mathcal{A}(\mathbf{u})$ is nonempty. Using Proposition 7 in (Gunawardana and Byrne, 2005), we can further show that the point-to-set mapping \mathcal{A} is closed at $\mathbf{u} \in \mathcal{U}$. Condition 3 is satisfied.

For each \mathbf{u}^k , \mathbf{u}^{k+1} is the solution of $\mathcal{F}(\mathbf{u})$ and $\mathcal{A}(\mathbf{u})$ is a closed mapping, therefore each \mathbf{u}^{k+1} belongs to a compact set. We know that the union of two compact sets is compact. Therefore, all points $\{\mathbf{u}^k\}$ are contained in a compact set $S \in \mathcal{U}$. Condition 1 is satisfied.

To prove condition 2, we must show that for any \mathbf{u}^k , $\mathcal{L}(\mathbf{u}^{k+1}) < \mathcal{L}(\mathbf{u}^k)$ for all $\mathbf{u}^{k+1} \in \mathcal{A}(\mathbf{u}^k)$ if $\mathbf{u}^k \notin \Gamma$; $\mathcal{L}(\mathbf{u}^{k+1}) \leq \mathcal{L}(\mathbf{u}^k)$ for all $\mathbf{u}^{k+1} \in \mathcal{A}(\mathbf{u}^k)$ if $\mathbf{u}^k \in \Gamma$. At any \mathbf{u}^k , the auxiliary cost function $\mathcal{F}(\mathbf{u})$ (eq. 35) is strictly tangent to $\mathcal{L}(\mathbf{u})$ at \mathbf{u}^k . Therefore, if $\mathbf{u}^k \notin \Gamma$, $\mathcal{L}(\mathbf{u}^k) = \mathcal{F}(\mathbf{u}^k) > \mathcal{F}(\mathbf{u}^{k+1}) \geq \mathcal{L}(\mathbf{u}^{k+1})$, thus $\mathcal{L}(\mathbf{u}^k) > \mathcal{L}(\mathbf{u}^{k+1})$; if $\mathbf{u}^k \in \Gamma$, $\mathcal{L}(\mathbf{u}^k) = \mathcal{F}(\mathbf{u}^k) = \mathcal{F}(\mathbf{u}^{k+1}) \geq \mathcal{L}(\mathbf{u}^{k+1})$, thus $\mathcal{L}(\mathbf{u}^k) \geq \mathcal{L}(\mathbf{u}^{k+1})$. Condition 2 is satisfied. \blacksquare

The algorithm could theoretically converge to a saddle point, but any minimal perturbation would easily lead to escape.

4.1.3 DECOUPLED LAPLACE APPROXIMATION

To optimize marginal likelihood for the DRD hyperparameters (eq. 23), we should ideally replace $\mathbf{m}_{\mathbf{u}}$ and $\Lambda_{\mathbf{u}}$ with explicit expressions in $\boldsymbol{\theta}$ in order to accurately compute derivatives with respect $\boldsymbol{\theta}$. However, the deterministic formulation of such functions is intractable. We can nevertheless partially overcome this dependence by introducing a “decoupled” Laplace approximation that takes account of the dependence of $\Lambda_{\mathbf{u}}$ on the hyperparameters $\boldsymbol{\theta}_{drd}$. Specifically, we rewrite the inverse Laplace posterior covariance (eq. 22):

$$\Lambda_{\mathbf{u}} = (\Gamma + \Psi(\boldsymbol{\theta}_{drd}))^{-1} \quad (36)$$

where Γ is the negative Hessian of the log-likelihood (which is independent of $\boldsymbol{\theta}_{drd}$),

$$\Gamma = -\frac{\partial^2}{\partial \mathbf{u} \partial \mathbf{u}^\top} \log p(\mathbf{y}|X, \mathbf{u}, \sigma^2, \delta), \quad (37)$$

and $\Psi(\boldsymbol{\theta}_{drd})$ is the precision matrix of the prior distribution for \mathbf{u} ,

$$\Psi(\boldsymbol{\theta}_{drd}) = -\frac{\partial^2}{\partial \mathbf{u} \partial \mathbf{u}^\top} \log p(\mathbf{u}|\boldsymbol{\theta}_{drd}) = K^{-1}, \quad (38)$$

which is the inverse of the GP prior covariance governing \mathbf{u} (eq. 7). Substituting for $\Lambda_{\mathbf{u}}$ in (eq. 23), this gives:

$$\log p(\mathbf{y}|X, \boldsymbol{\theta}) \approx \log p(\mathbf{y}|X, \mathbf{m}_{\mathbf{u}}, \sigma^2, \delta) + \log p(\mathbf{m}_{\mathbf{u}}|\boldsymbol{\theta}_{drd}) - \frac{1}{2} \log |\Gamma + K^{-1}| + \text{const}. \quad (39)$$

This form decomposes the curvature at the posterior mode into the likelihood curvature and prior curvature. In this way, the posterior curvature tracks the influence of the change in prior curvature as we optimize the hyperparameters $\boldsymbol{\theta}$, while keeping the influence of the likelihood curvature fixed. This decoupling allows us to update the posterior without

Algorithm 2 Evidence optimization using decoupled Laplace approximation

Input: X, \mathbf{y} **Output:** latents $\hat{\mathbf{u}}$, hyperparameters $\hat{\boldsymbol{\theta}}$.At iteration t :

1. Numerically optimize log-posterior for latents $\mathbf{m}_{\mathbf{u}}^t$ using (eq. 19) or Algorithm 1.
 2. Compute Γ^t using negative Hessian of the log conditional evidence (eq. 37).
 3. Numerically optimize $p(\mathbf{y}|X, \boldsymbol{\theta}, \mathbf{m}_{\mathbf{u}}^t, \Gamma^t)$ (eq. 39) for $\boldsymbol{\theta}^t$.
- Repeat step 1, 2 and 3 until $\{\mathbf{m}_{\mathbf{u}}, \Gamma\}$ and $\boldsymbol{\theta}$ converge.
-

recomputing the Hessian. It will be accurate so long as the Hessian of the likelihood changes slowly over local regions in parameter space.

To optimize hyperparameters under the decoupled Laplace approximation, we fix $\mathbf{m}_{\mathbf{u}}$ and Γ using the current mode of the posterior, and optimize (eq. 39) directly for $\boldsymbol{\theta}$, incorporating the dependence of K on $\boldsymbol{\theta}_{drd}$. With this approach, the first term, $\log p(\mathbf{y}|X, \mathbf{m}_{\mathbf{u}}, \sigma^2, \delta)$, captures the dependence on σ^2 and δ ; the second term, $\log p(\mathbf{m}_{\mathbf{u}}|\boldsymbol{\theta}_{drd})$, restricts $\boldsymbol{\theta}_{drd}$ around the current mode; and the third term $-\frac{1}{2} \log |\Gamma + K^{-1}|$ pushes $\boldsymbol{\theta}_{drd}$ along the second order curvature given the GP kernel. This decoupling weakens the strong dependency between $\boldsymbol{\theta}_{drd}$ and $\mathbf{m}_{\mathbf{u}}$, maintaining the accuracy of the Laplace approximation as we adjust $\boldsymbol{\theta}_{drd}$.

To ensure accuracy of the Laplace approximation, in each iteration t , we optimize eq. (39) over a restricted region of the hyperparameter space around the previous hyperparameter setting $\boldsymbol{\theta}^{t-1}$, which allows to vary within 20% of its current value on each iteration in our experiments. This prevents $\boldsymbol{\theta}$ from moving too far from the region where the current Laplace approximation ($\mathbf{m}_{\mathbf{u}}$ and Γ) is accurate. Then, based on a new hyperparameter setting $\boldsymbol{\theta}^t$, we update the Laplace approximation parameters $\mathbf{m}_{\mathbf{u}}$ and Γ . This procedure is summarized in Algorithm 2. The algorithm stops when $\{\mathbf{m}_{\mathbf{u}}, \Gamma\}$ and $\boldsymbol{\theta}$ converge. The empirical Bayes estimate is then given by the MAP estimate of the weights $\mathbf{w}_{map} = \boldsymbol{\mu}_{\mathbf{w}}$ (eq. 12) conditioned on the optimal latents $\hat{\mathbf{u}} = \mathbf{m}_{\mathbf{u}}$ and hyperparameters $\hat{\boldsymbol{\theta}}$.

4.2 Fully Bayesian inference with MCMC

An alternate approach to the empirical Bayesian inference procedure described above is to perform fully Bayesian inference using Markov Chain Monte Carlo (MCMC). Using sampling, we can compute the integrals over \mathbf{u} and $\boldsymbol{\theta}$ in order to compute the posterior mean (Bayes' least squares estimates) for \mathbf{w} . The full posterior distribution over \mathbf{w} can be written

$$p(\mathbf{w}|X, \mathbf{y}) = \iint p(\mathbf{w}|X, \mathbf{y}, \mathbf{u}, \boldsymbol{\theta}) p(\mathbf{u}, \boldsymbol{\theta}|X, \mathbf{y}) d\mathbf{u} d\boldsymbol{\theta} \quad (40)$$

$$= \iint \mathcal{N}(\mathbf{w}|\boldsymbol{\mu}_{\mathbf{w}}, \Lambda_{\mathbf{w}}) p(\mathbf{u}, \boldsymbol{\theta}|X, \mathbf{y}) d\mathbf{u} d\boldsymbol{\theta}, \quad (41)$$

where mean $\mu_{\mathbf{w}}$ and covariance $\Lambda_{\mathbf{w}}$ are functions of \mathbf{u} and $\boldsymbol{\theta}$ (eq. 12). This suggests a Monte Carlo representation of the posterior as

$$p(\mathbf{w}|X, \mathbf{y}) = \frac{1}{N} \sum_{i=1}^N \mathcal{N}\left(\mathbf{w} \mid \mu_{\mathbf{w}}(\mathbf{u}^{(i)}, \boldsymbol{\theta}^{(i)}), \Lambda_{\mathbf{w}}(\mathbf{u}^{(i)}, \boldsymbol{\theta}^{(i)})\right) \quad (42)$$

$$\mathbf{u}^{(i)}, \boldsymbol{\theta}^{(i)} \sim p(\mathbf{u}, \boldsymbol{\theta}|X, \mathbf{y}), \quad (43)$$

where i is the index of the samples and N is the total number of samples. We can use Gibbs sampling to alternately sample \mathbf{u} and $\boldsymbol{\theta}$ from their conditional distributions given the other. The joint posterior distribution of \mathbf{u} and $\boldsymbol{\theta}$ has the following proportional relationship,

$$p(\mathbf{u}, \boldsymbol{\theta}|X, \mathbf{y}) \propto p(\mathbf{y}|X, \mathbf{u}, \sigma^2, \delta) p(\mathbf{u}|\boldsymbol{\theta}_{drd}) \text{Prior}(\boldsymbol{\theta}), \quad (44)$$

where $p(\mathbf{y}|X, \mathbf{u}, \sigma^2, \delta)$ and $p(\mathbf{u}|\boldsymbol{\theta}_{drd})$ have the likelihoods given in (eq. 20) and (eq. 21), and $\text{Prior}(\boldsymbol{\theta})$ is the prior distribution for $\boldsymbol{\theta}$.

Sampling latents $\mathbf{u}|\boldsymbol{\theta}$

The first phase of Gibbs sampling is to sample \mathbf{u} from the conditional distribution of \mathbf{u} given $\boldsymbol{\theta}$,

$$\mathbf{u}|\boldsymbol{\theta} \sim p(\mathbf{y}|X, \mathbf{u}, \sigma^2, \delta) p(\mathbf{u}|\boldsymbol{\theta}_{drd}). \quad (45)$$

This is the product of a Gaussian process prior $p(\mathbf{u}|\boldsymbol{\theta}_{drd})$ and a likelihood function $p(\mathbf{y}|X, \mathbf{u}, \boldsymbol{\theta})$ that ties the latent variables \mathbf{u} to the observed data. This setting meets the requirements of elliptical slice sampling (ESS), a rejection-free MCMC (Murray et al., 2009). ESS generates random elliptical loci using the Gaussian prior and then searches along these loci to find acceptable points by evaluating the data likelihood. This method takes into account strong dependencies imposed by GP covariance on the elements of the vector \mathbf{u} to facilitates faster mixing. It also requires no tuning parameters, unlike alternative samplers such as Metropolis-Hastings or Hamiltonian Monte Carlo, but performs similarly to the best possible performance of a related M-H scheme. To overcome slow mixing that can result when the prior covariance is highly elongated, we apply ESS to a whitened variable using a reparametrization trick, discussed in more detail in Sec. 4.3.

Sampling hyperparameters $\boldsymbol{\theta}|\mathbf{u}$

The conditional distribution for sampling $\boldsymbol{\theta}$ given \mathbf{u} is

$$\boldsymbol{\theta}|\mathbf{u} \sim p(\mathbf{y}|X, \mathbf{u}, \sigma^2, \delta) p(\mathbf{u}|\boldsymbol{\theta}_{drd}) \text{Prior}(\boldsymbol{\theta}), \quad (46)$$

where $\boldsymbol{\theta} = \{\sigma^2, b, \rho, l, \delta\}$ contains five individual hyperparameters. We therefore perform slice sampling for each variable conditioned on the others. We use prior distributions of the form:

$$\log(\sigma^2) \sim \mathcal{N}(m_n, \sigma_n^2), \quad b \sim \mathcal{N}(m_b, \sigma_b^2), \quad \rho \sim \Gamma(a_\rho, b_\rho), \quad l \sim \Gamma(a_l, b_l), \quad \delta \sim \Gamma(a_\delta, b_\delta). \quad (47)$$

We put a Gaussian prior on the log of σ^2 instead of σ^2 . We will provide the values for these priors in the Sec. 5 on synthetic experiments .

4.3 Whitening the GP prior using reparametrization

In both Laplace approximation and MCMC frameworks, the latent vector \mathbf{u} depends on the product of the conditional evidence $p(\mathbf{y}|X, \mathbf{u}, \sigma^2, \delta)$ and the GP prior $p(\mathbf{u}|\boldsymbol{\theta}_{drd})$. The GP prior (which is the primary difference between our model and standard ARD) introduces strong dependencies between \mathbf{u} and GP hyperparameters, resulting in a highly elliptical joint distribution. Such distributions are often problematic for both optimization and sampling. For example, if we are trying to perform Gibbs sampling on \mathbf{u} and the GP length scale hyperparameter l and the prior is strong relative to the evidence term, the samples $\mathbf{u}^{(i)}$ will have smoothness strongly determined by $l^{(i)}$, and the samples $l^{(i)}$ will in turn be strongly determined by smoothness of the current sample $\mathbf{u}^{(i)}$. In this case, mixing will be slow, and Gibbs sampling will take a long time to explore the full posterior over different values of l .

We can overcome this difficulty with a technique known as the “reparametrization trick”, which involves reparameterizing the model so that the unknown variables are independent under the prior (Murray and Adams, 2010). If we have prior $P(\mathbf{u}) = \mathcal{N}(b\mathbf{1}, K)$, then \mathbf{u} can be described equivalently by a deterministic transformation of standard normal random variable \mathbf{v} :

$$\mathbf{v} \sim \mathcal{N}(0, I), \quad \mathbf{u} = L\mathbf{v} + b\mathbf{1}, \quad (48)$$

where $K = LL^\top$ is the Cholesky factorization of prior covariance K .

This reparametrization simplifies Laplace-approximation-based inference by allowing a change of variables in (eq. 19) so that we directly maximize $p(\mathbf{y}|X, \mathbf{v}, \boldsymbol{\theta})\mathcal{N}(\mathbf{v}|0, I)$ for \mathbf{v} . This optimization problem has better conditioning, and eliminates the computational problem of computing $\mathbf{u}^\top K^{-1}\mathbf{u}$ in the log prior, which is replaced by a simple ridge penalty of the form $\mathbf{v}^\top \mathbf{v}$.

For sampling-based inference, the reparametrization allows us to improve mixing performance because the conditionals $\mathbf{v}|\boldsymbol{\theta}$ and $\boldsymbol{\theta}|\mathbf{v}$ exhibit much weaker dependencies than $\mathbf{u}|\boldsymbol{\theta}$ and $\boldsymbol{\theta}|\mathbf{u}$. Moreover, elliptical slice sampling for $\mathbf{v}|\boldsymbol{\theta}$ is more efficient because it involves loci on a sphere instead of a highly elongated ellipsoid.

4.4 Fourier dual form

A second trick for improving the computational performance of DRD is to perform optimization of the latent variable \mathbf{u} (or \mathbf{v}) in the Fourier domain. When the GP prior induces a high degree of smoothness in \mathbf{u} , the prior covariance K becomes approximately low rank, meaning that it has a small number of non-negligible eigenvalues. Because the covariance function (eq. 7) is shift invariant, the eigenspectrum of K has a diagonal representation in the Fourier domain, a consequence of Bochner’s theorem (Stein, 1999; Lázaro-Gredilla et al., 2010). We can exploit this representation to optimize $\tilde{\mathbf{u}}$, the discrete Fourier transform of \mathbf{u} , while ignoring Fourier components above a certain high-frequency cutoff, where this cutoff depends on the length scale l . This results in lower-dimensional optimization problem. Fourier-domain representation of the latent vector \mathbf{u} also simplifies the application of the reparametrization trick described above because the Cholesky factor L is

now a diagonal matrix that can be computed analytically from the spectral density of the squared-exponential prior.

To summarize the joint application of the reparametrization and Fourier dual tricks in our model, they can be understood as allowing us to draw samples $\mathbf{u} \sim \mathcal{N}(b\mathbf{1}, K)$ via the series of transformations:

$$\tilde{\mathbf{v}} \sim \mathcal{N}(0, I), \quad \text{whitened Fourier domain sample} \quad (49)$$

$$\tilde{\mathbf{u}} = L\tilde{\mathbf{v}} + \tilde{\mathbf{b}}, \quad \text{transformed Fourier domain sample} \quad (50)$$

$$\mathbf{u} = B\tilde{\mathbf{u}}, \quad \text{inverse Fourier transform} \quad (51)$$

where $\tilde{\mathbf{b}}$ is the discrete Fourier transform of $b\mathbf{1}$, a vector of zeros except for a single non-zero element carrying the DC component, and B is the truncated (tall skinny) discrete inverse Fourier transform matrix mapping the low-frequency Fourier components represented in $\tilde{\mathbf{u}}$ to the space domain.

Note that the smoothness on \mathbf{u} , which controls the spatial scale of dependent sparsity, is different from the smoothing prior used in smooth-DRD to induce smoothness in the coefficients \mathbf{w} , although both can benefit from sparse Fourier-domain representation in cases where the relevant length scale is large.

5. Synthetic experiments

5.1 Simulated example with smooth and sparse weights

To illustrate and give intuition for the performance of the DRD estimator, we begin with a simulated experiment using a vector of regression weights embedded in a one-dimensional space. We sampled a $p = 4000$ dimensional weight vector \mathbf{w} from the smooth-DRD prior (see Fig. 1), with hyperparameters GP mean $b = -8$, GP length scale $l = 100$, GP marginal variance $\rho = 36$, smoothness length scale $\delta = 50$, measurement noise variance $\sigma^2 = 5$. We then sampled responses $n = 500$ responses $\mathbf{y} = X\mathbf{w} + \epsilon$, where X is a $n \times p$ design matrix with entries drawn i.i.d. from a standard normal distribution, and noise $\epsilon_i \sim \mathcal{N}(0, 5)$.

Fig. 3 displays an example of a true coefficient vector \mathbf{w}_0 , and shows a comparison to a variety of different estimators:

- lasso (Tibshirani, 1996), implemented with using Least Angle Regression (LARS) implemented by glmnet¹;
- automatic relevance determination (ARD) (Neal, 1995; MacKay, 1992), implemented with the classic fixed point algorithm.
- automatic smoothness determination (ASD) (Sahani and Linden, 2003), which uses numerical optimization of marginal likelihood to learn the hyperparameters of a squared exponential kernel governing \mathbf{w} .

1. https://web.stanford.edu/~hastie/glmnet/glmnet_alpha.html

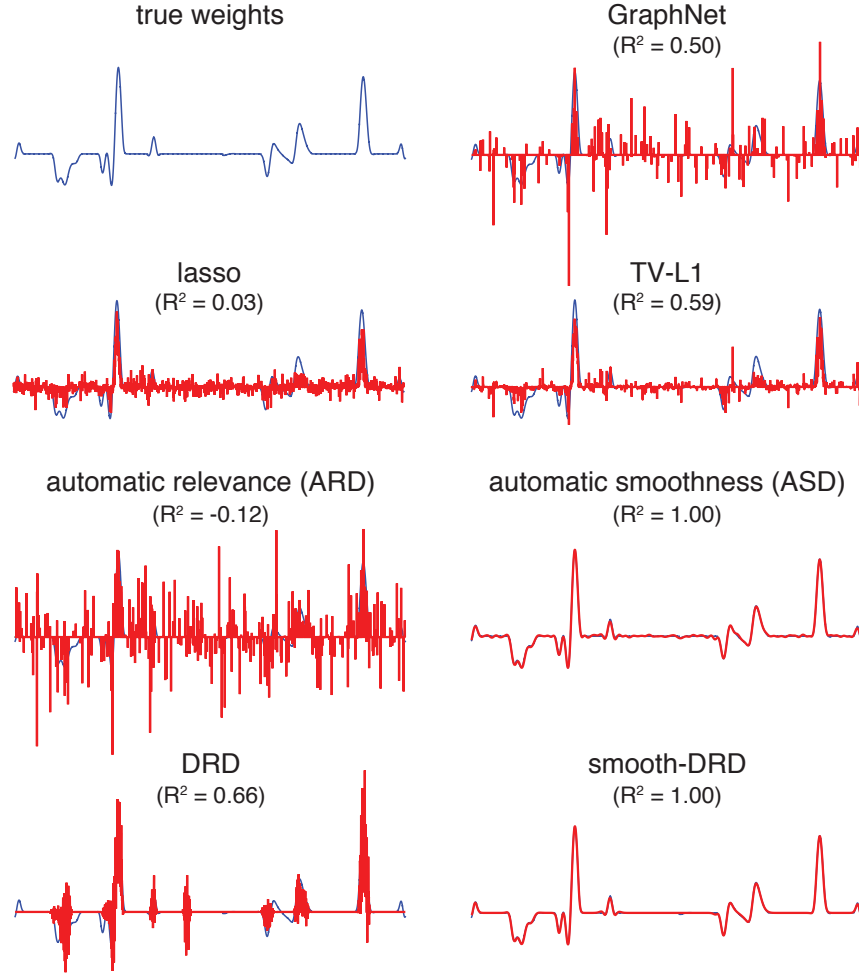


Figure 3: True signal \mathbf{w}_0 and the different reconstructions generated by each method for one instance of the signal reconstruction problem. The title of each subfigure includes the R^2 values for \mathbf{w} and the test set. For DRD models, we only present DRD-Laplace and smooth-DRD-Laplace. The other DRD based models present similar estimations and R^2 values.

- total variation l_1 (TV-L1) (Michel et al., 2011; Baldassarre et al., 2012; Gramfort et al., 2013), which combines total variation penalty (also known as fused lasso), which imposes an l_1 penalty on the first-order differences of \mathbf{w} , with a standard lasso penalty.
- graph net (GraphNet) (Grosenick et al., 2011), a graph-constrained elastic net, developed for spatial and temporally correlated data that yields interpretable model parameters by incorporating sparse graph priors based on model smoothness or connectivity, as well as a global sparsity inducing prior that automatically selects important variables.

We computed total variation l_1 (TV-L1) and graph net (GraphNet) estimates using the Nilearn² package. Cross-validation was used to set hyperparameters in all the above methods (except for ARD and ASD, which use evidence optimization).

For the DRD model, which incorporates structured sparsity but not smoothness, we compared three different inference methods: (1) Laplace approximation based inference (“DRD-Laplace”); (2) Markov Chain Monte Carlo (“DRD-MCMC”); and (3) Convex relation based optimization (“DRD-Convex”). Lastly, for the smooth-DRD model, we used two inference methods: (4) Laplace approximation (“smooth-DRD-Laplace”); and (5) MCMC (“smooth-DRD-MCMC”). For optimization based DRD estimators, we initialized $\tilde{\mathbf{v}}$ with a very small value at 10^{-3} scale in the first iteration to estimate \mathbf{u} . The hyper-hyperparameters in the MCMC methods (eq. 47) were set to: $m_n = -2, \sigma_n^2 = 5, m_b = -10, \sigma_b^2 = 8, a_\rho = 4, b_\rho = 5, a_l = 4, b_l = 25, a_\delta = 4, b_\delta = 25$.

Fig. 3 shows a comparison between the above estimators on a simulated example, revealing that the smooth-DRD estimate performed best for recovering \mathbf{w} . The ASD estimate also achieved high reconstruction performance in terms of R^2 , although the estimate is not sparse, carrying small wiggles where the coefficients should be zero. The standard DRD estimate recovered the support of \mathbf{w} with high accuracy, but had larger error than smooth-DRD estimates due to the smoothness of the true \mathbf{w} . The other methods (lasso, ARD, TV-L1 and GraphNet) all had lower accuracy in recovering both the support and values of the regression weights.

To gain insight into the DRD estimates, we also plotted the prior covariance of the weights \mathbf{w} conditioned on the optimized hyperparameter values for the ARD, DRD, and smooth-DRD models (Fig. 4). Although DRD and smooth-DRD both reside in the ARD framework, meaning that they achieve sparsity by shrinking the prior variance of unnecessary coefficients to zero, their covariances both exhibit local clusters of non-zero coefficients. This reflects the dependencies introduced by the latent Gaussian process, and is noticeably absent from the ARD prior covariance. Note that ARD and DRD covariances are both diagonal, making the weights independent given the prior variances, whereas the smooth-DRD covariance also has off-diagonal elements that enforce smoothness.

To compare the different estimators quantitatively, we performed repeated experiments using data drawn from the DRD generative model. For each experiment, we generated simulated data with $n = 500$ samples from a $p = 4000$ element weight vector, with hyperparameters as given above. To examine performance as a function of training set size, we randomly split data into training and test sets with training set size ranging from 100 to 400. We note that even with $n = 500$ samples, the problem resides in the small-sample regime.

Fig. 5 shows the reconstruction performance (R^2) for different estimators as a function of training set size. The reconstruction performance for recovering the true \mathbf{w}_0 is given by $R^2 = 1 - \frac{\|\mathbf{w}_0 - \hat{\mathbf{w}}\|_2^2}{\|\mathbf{w}_0 - \bar{\mathbf{w}}_0\|_2^2}$, where $\|\cdot\|_2$ denotes the l_2 -norm and $\hat{\mathbf{w}}$ is the corresponding estimate of the signal \mathbf{w}_0 . Solid lines show the average reconstruction R^2 and the shaded area indicates the standard deviation over six repeated experiments. We found that the

2. <http://nilearn.github.io/index.html>

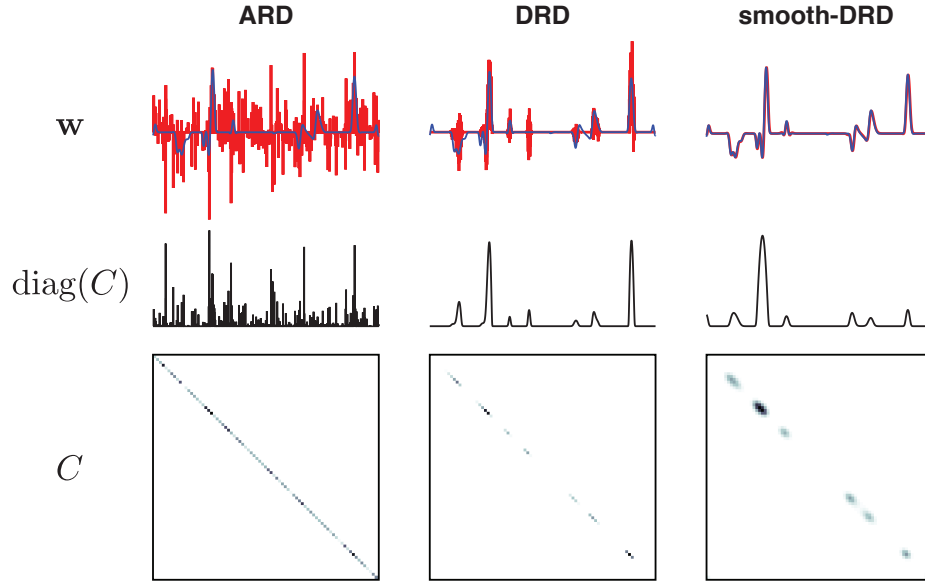


Figure 4: Estimated filter weights and prior covariances. The upper row shows the true filter (blue) and estimated ones (red); the middle row displays the diagonal of each estimated covariance matrix; and the bottom row shows the entire estimated covariance matrix for each prior.

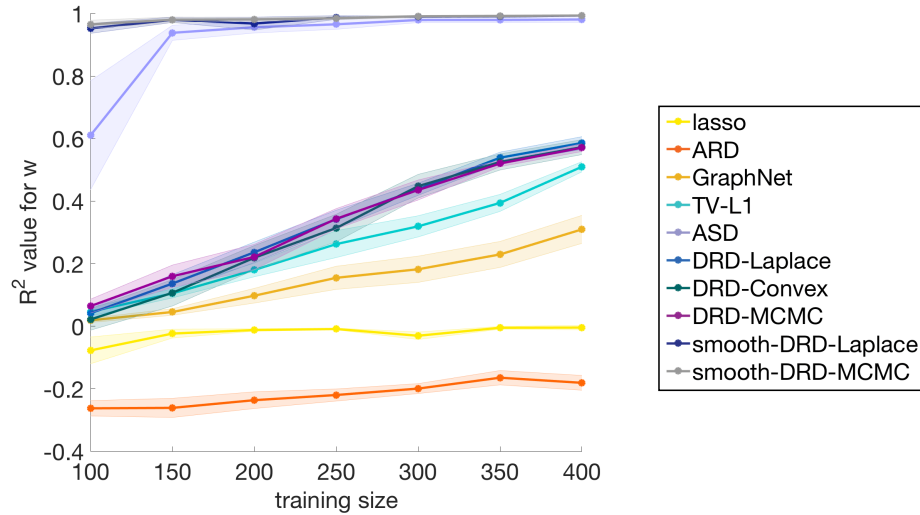


Figure 5: Average reconstruction R^2 values on the signal reconstruction problem as a function of the number of training measurements performed for lasso, ARD, GraphNet, TV-L1, ASD and our DRD based methods. The x-axis is the training size and the y-axis is the R^2 criterion.

Laplace and MCMC estimates for the smooth-DRD model outperformed other estimators and were approximately equally accurate, indicating that use of Laplace approximation did not noticeably harm performance relative to the fully Bayesian estimate. Also surprisingly, smooth-DRD estimators achieved nearly perfect reconstruction performance over all the training sizes, even at the smallest training set size of $n = 100$. The next best performance was achieved by the ASD estimator, which was comparable to the smooth-DRD estimates at larger training set sizes. Amongst estimators that did not exploit smoothness, the plain DRD estimates outperformed all the others methods. However, the superior accuracy of ASD indicates that for these extremely smooth weights, smoothness is a more useful form of regularization than structured sparsity conferred by DRD.

Overall, smooth-DRD outperformed all other methods. This shows that combining sparsity and smoothness can provide major advantages over methods that impose only one or the other. This flexible framework for integrating structured sparsity and smoothness is one of the primary contributions of our work, in contrast to previous methods in the structured sparsity literature which consider only sparsity.

5.2 Comparison of DRD optimization methods

We have discussed three different estimators for the DRD model: optimization-based inference under the Laplace approximation, sampling-based inference using MCMC, optimization-based inference under a two-stage convex relaxation of the Laplace approximation. The standard Laplace method is the fastest, but it is prone to getting stuck in local optima. The MCMC estimator does not suffer from local optima, but is computationally expensive due to the cost of burn-in and generating many samples of the posterior. The two-stage convex relaxation approach attempts to improve on the standard Laplace estimator by maximizing a convex upper on the log-likelihood. Although the full optimization problem is still non-convex, this approach employs a series of convex optimizations in place of numerical ascent of the non-convex log-likelihood, and we find empirically that it exhibits better convergence than the standard Laplace estimator.

Although the DRD-Laplace and DRD-convex exhibited performance in terms of R^2 on simulated data (Fig. 5), we found that the convex estimator exhibited faster convergence. Fig. 6 illustrates the convergence behavior of the DRD-Laplace and DRD-Convex estimators over 200 iterations with the same initialization, showing that the convex algorithm converges more rapidly, makes much smaller adjustments to the weights after the first few iterations.

6. Phase transition in sparse signal recovery

Compressive sensing focuses on the recovery of sparse high-dimensional signals in settings where the number of signal coefficients p exceeds the number of measurements n . Recent work has shown that the recovery of sparse signals exhibits a phase transition between perfect and imperfect recovery as a function of the number of measurements (Ganguli and Sompolinsky, 2010; Amelunxen et al., 2014). Namely, when the measurement fraction $\gamma = n/p$ exceeds some critical value that depends on signal sparsity, the signal can be

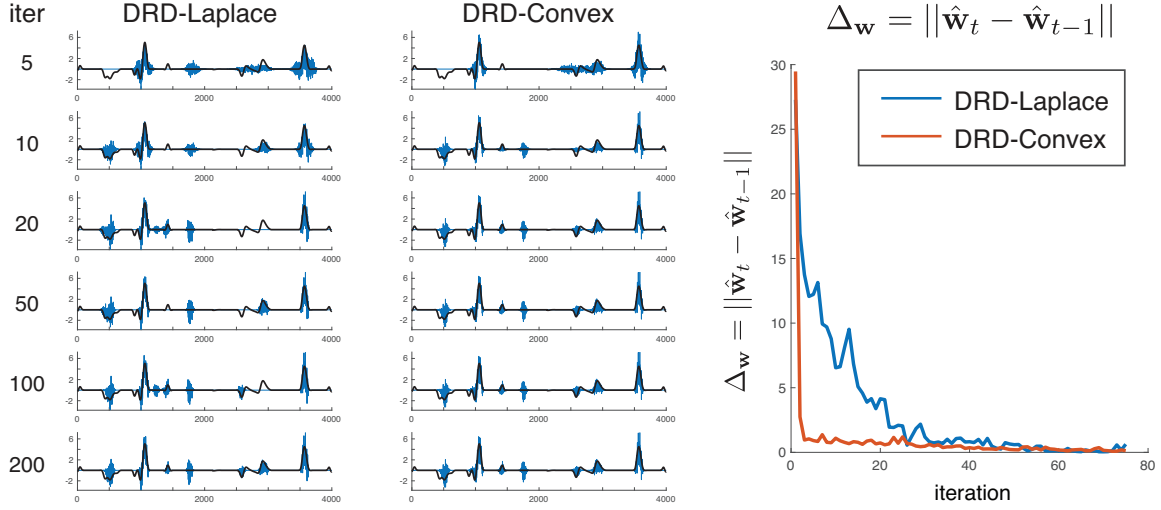


Figure 6: Comparison of the optimization of weights $\hat{\mathbf{w}}$ between DRD-Laplace and DRD-Convex. The first two columns show the weights obtained after 5, 10, 20, 50, 100, and 200 iterations under the two estimators, with true weights indicated in black. The third column shows the change in weights after each iteration of the standard and convex optimization algorithms over the first 80 iterations, showing that the convex algorithm converges more rapidly, makes much smaller adjustments to the weights after the first few iterations.

recovered perfectly with probability approaching 1, whereas for γ below this value, estimates contain errors with probability approaching 1. However, these results were derived for the case where non-zero coefficients are randomly located within the signal vector. Here we show that DRD can obtain dramatic improvements over the phase transition curve for *iid* sparse signals when the non-zero coefficients arise in clusters.

We performed simulated experiments to examine the effects of group structure on the empirical phase transition between perfect and imperfect recovery of sparse signals. The measurement equation is given by the noiseless version of the linear system we have considered so far: $\mathbf{y} = X\mathbf{w}$, where $\mathbf{w} \in \mathbb{R}^p$ is the sparse signal, $\mathbf{y} \in \mathbb{R}^n$ is the (dense) measurement vector, and here $X \in \mathbb{R}^{n \times p}$ is a (short, fat) random measurement matrix with entries drawn *iid* from a standard normal distribution. We define the sparsity of the signal as $\alpha = k/p$, where k is the number of non-zero signal coefficients in \mathbf{w} .

To explore the effects of group structure, we considered the signal coefficients in \mathbf{w} to have 1D spatial structure and introduced a parameter g specifying the number of spatial groups or clusters into which the non-zero coefficients were divided. When $g = 1$, the non-zero coefficients formed a single contiguous block of length k , with location uniformly distributed within \mathbf{w} . When $g > 2$, the non-zero coefficients were divided into g blocks of size k/g , and the locations of these blocks are uniformly distributed within \mathbf{w} subject to

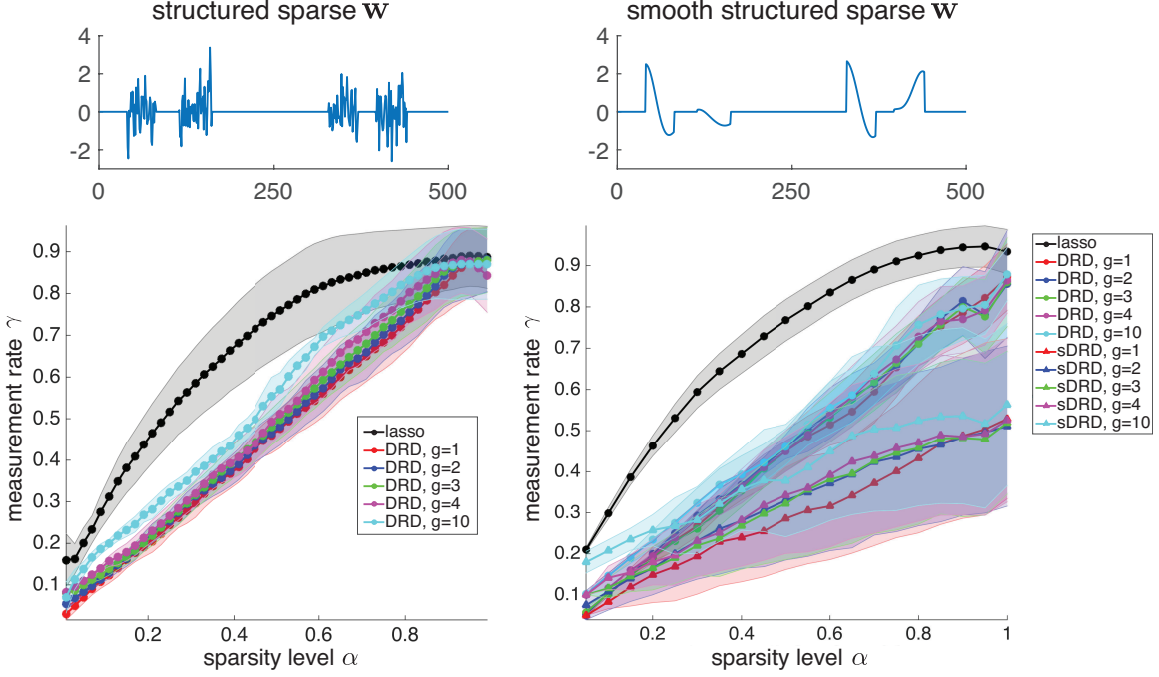


Figure 7: **Phase transitions for DRD and smooth-DRD (sDRD) estimators on signals with structured sparsity.** Top two rows show example signals \mathbf{w} of dimension $p = 500$, which contain randomly positioned blocks of non-zero coefficients. Non-zero coefficients were clustered into varying numbers of groups g , and drawn either iid from a standard normal distribution (left column) or from a Gaussian process with length scale 20 (right column), to illustrate the effects of smoothness. To compute phase transition curves, we analyzed the recovery behavior of each estimator at every point in a 2D grid of sparsity levels α and measurement rates γ . At each point, we generated 10 random signals \mathbf{w} , projected them noiselessly onto a random Gaussian measurement matrix X , and computed lasso and DRD estimates $\hat{\mathbf{w}}$. We then calculated the R^2 value of the estimates for each trial at every grid point (α, γ) . An estimator was considered to achieve perfect recovery if all 10 trials resulted in $R^2 > 0.95$, and perfect failure if all 10 trials resulted in $R^2 \leq 0.95$; remaining points were considered to fall in the phase transition region. For each estimator, the shaded region indicates the phase transition region, and solid line indicates its center of mass along the y-axis.

the constraint that blocks remain disjoint. Once the sparsity pattern was determined, we sampled the non-zero coefficients from a standard normal distribution.

Fig. 7 shows the empirical phase transition curves for lasso and DRD estimators for sparse signals with non-zero coefficients clustered into varying numbers of groups g . These curves show the boundary between perfect and imperfect signal recovery for different estimators

in the 2D space of signal sparsity level α and measurement fraction γ . The left bottom plot shows that DRD estimators achieved perfect signal recovery for much lower measurement rates, even when non-zero coefficients were clustered into as many as 10 groups. Here DRD achieved transition to perfect recovery along the main diagonal, whereas lasso exhibited an arc-shape transition curve described previously (Ganguli and Sompolinsky, 2010; Amelunxen et al., 2014), indicating that more measurements were required to recovery signals of equal sparsity. In the right bottom plot, we generated the non-zero coefficients from a Gaussian process with length scale equal to 20, so that non-zero coefficients were smooth as well as sparse. In these plots, we compared lasso estimates (which do not benefit from group or smooth structure) to standard DRD and smooth-DRD estimates. This revealed that smoothness allowed for further reductions in measurement rates, with perfect signal recovery achievable well below that of the non-smooth DRD estimates.

7. Applications to brain imaging data

Functional magnetic resonance imaging (fMRI) measures blood oxygenation levels, which provide a proxy for neural activity in different parts of the brain. Although these measurements are noisy and indirect, fMRI is one of the primary non-invasive methods for measuring activity in human brains, and it has provided insight into the neural basis for a wide variety of cognitive abilities and functional pathologies.

A primary problem of interest in the fMRI literature is “decoding”, which involves the use of linear classification and regression methods to identify the stimulus or behavior associated with measured brain activity. Decoding is a challenging statistical problem because the number of volumetric pixels or “voxels” measured with fMRI is typically far greater than the number of trials in an experiment; a full brain volume typically contains 50K voxels whereas most experiments produce only a few hundred observations.

Standard approaches to decoding have therefore tended to exploit sparsity, corresponding to the assumption that only a small set of brain voxels are relevant for decoding a particular set of stimuli (Carroll et al., 2009). However, the set of voxels useful for a specific decoding task are not randomly distributed throughout the brain, but tend to arise in clusters; if one voxel carries information useful for decoding, it is *a priori* likely that nearby voxels do too, given that voxels represent an arbitrary discretization of continuous underlying brain structures. We therefore explored brain decoding as an ideal application for evaluating the performance of our estimators.

7.1 Gambling task

We first considered the regression problem of decoding gains and losses from fMRI measurements recorded in a gambling task (Tom et al., 2007, 2011). In this experiment, event-related fMRI was administered while healthy human participants performed a decision-making task. In each trial, a gamble with a potential gain and loss (each with 50% probability) was presented for 3s, and the participants were instructed to decide whether to accept or reject the gamble. Experimenters varied amount of the potential gain and loss across trials.

After standard preprocessing, the regression dataset consisted of 16 subjects with 48 fMRI measurements per subject (resulting from 6 repeated presentations of 8 different gambles). fMRI measurements were obtained from a 3D brain volume of $40 \times 48 \times 34$ voxels, each of size $4 \times 4 \times 4$ mm, from which a subset of 33,177 valid brain voxels were used for analysis. The full dataset of 16 subjects therefore contained $n = 768$ samples in a $p = 33,177$ dimensional space.

We evaluated inter-subject prediction performance by estimating regression weights with data from a subset of the 16 subjects, and computing prediction accuracy for data from held-out subjects. To assess the performance, we varied the train-test ratio in number of subjects from 9:7 to 13:3. We performed 10 different random train-test splits for each ratio. The curves in the top left panel of Fig. 8 show the performance of lasso, GraphNet, TV-L1 and DRD estimators. We found that DRD outperformed other estimators at nearly all train-test ratios, with a noticeable advantage at the largest training set size. However, we note that the SNR of this dataset was low, making inter-subject prediction difficult and resulting in low accuracy for all methods. A non-trivial preprocessing stage, such as hyper-alignment (Chen et al., 2015), could be used to map different subjects into a shared subspace, which might improve performance.

Fig. 8 also show the inferred regression weights for each estimator. The GraphNet and lasso weights had high sparsity, presumably due to the low SNR of the dataset, while TV-L1 weights exhibited small blocks of non-zero coefficients with constant value within each block, consistent with the structure expected for the TV-L1 penalty. The DRD weights were not sparse in a strict L0 sense, due to the fact that sparsity arises from soft-rectification of negative latents governing the prior variance. We therefore thresholded DRD weights for plotting purposes, revealing that the weights contributing most to prediction performance tended to cluster, as expected, although weights within each cluster were not constant.

7.2 Age prediction task

Next we considered the problem of predicting a subject’s age from a measured map of gray-matter concentration, using data from the Open Access Series of Imaging Studies (OASIS) (Marcus et al., 2007). The OASIS dataset consisted of T1-weighted MRI scans data from 403 subjects aged 18 to 96, with 3 or 4 scans per subject. One hundred of these subjects were over 60 years of age and had been clinically diagnosed with Alzheimer’s. The repeated scans provided high signal-to-noise ratio, making the dataset feasible for inter-subject analyses.

A natural regression problem for this dataset is to predict the age of subject from their anatomical data. The full dataset consisted of 403 samples with a $91 \times 109 \times 91$ 3D volume and 129,081 valid voxels. To assess the performance, we varied the training ratio from 0.4 to 0.8 out of the 403 subjects, and averaged over 5 random splits for each ratio.

The curves in the top left panel of Fig. 9 show mean absolute errors between the true age and the predicted age for each estimator, evaluated on test data. The DRD and smooth-DRD estimators, which performed similarly well, achieved lower error than lasso, GraphNet, and TV-L1 estimators. The inferred regression weights (Fig. 9) reveal that the most informative voxels for predicting age lie in thalamus and the basal ganglia; this is consistent with previ-

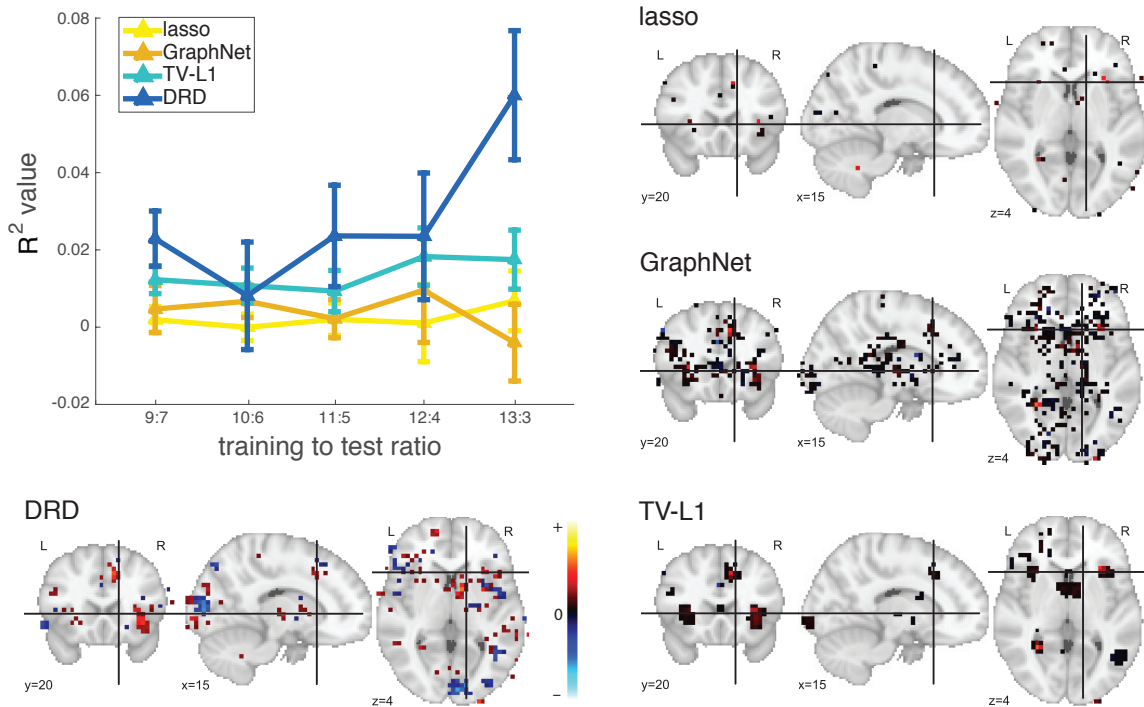


Figure 8: Top left panel shows average test R^2 values on the gambling dataset as a function of the train-test ratio for lasso, GraphNet, TV-L1 and DRD. The x-axis is the train-test split ratio and the y-axis is the R^2 criterion. The remaining panels show fMRI weight maps obtained, overlaid on a structural fMRI image. Colors indicate the sign and magnitude of the weights (see color bar). The DRD figure was obtained by cutting off small weight coefficients with a small threshold value at 0.004 (about 12% of the maximal absolute coefficient value).

ous findings about the relationship between Alzheimer’s disease progression and anatomical changes in gray matter (Cho et al., 2014; De Jong et al., 2008). Thalamus and basal ganglia were more clearly highlighted in the inferred DRD and smooth-DRD regression weights, which contained larger and more concentrated regions around these two structures. The smooth-DRD weights exhibited stronger spatial clustering than DRD weights, although regression performance was not noticeably different between the two estimators.

7.3 Visual recognition task

In a third application, we examined the problem of decoding faces and objects from fMRI measurements during a visual recognition task. We used a popular fMRI dataset from a study on face and object representation in human ventral temporal cortex (Haxby et al., 2001). In this experiment, 6 subjects were asked to recognize 8 different types of objects

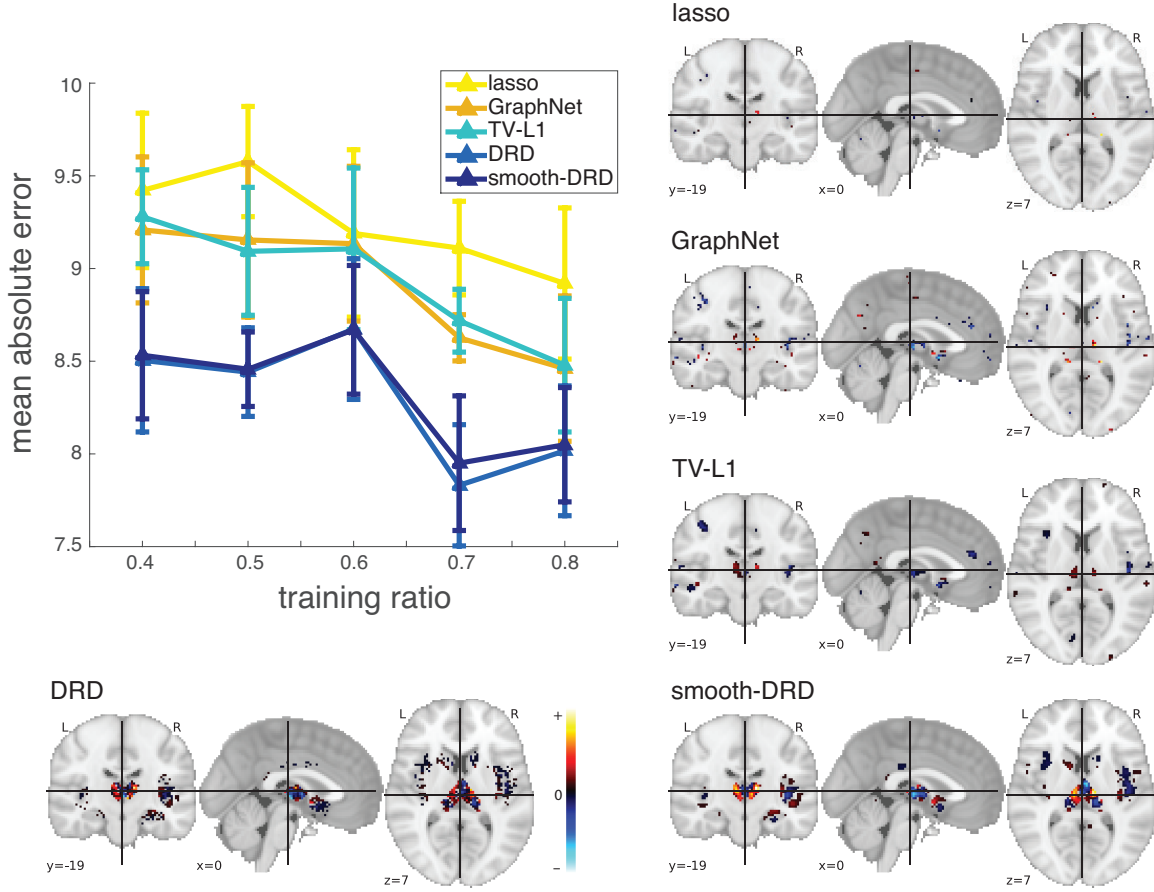


Figure 9: Top left panel shows average test mean absolute error values on the age regression dataset as a function of the training ratio for lasso, GraphNet, TV-L1, DRD and smooth-DRD. The x-axis is the ratio of the training data over the entire dataset and the y-axis is the mean absolute error criterion. The remaining panels show fMRI weight maps obtained, overlaid on a structural fMRI image. Colors indicate the sign and magnitude of the weights (see color bar).

(bottles, houses, cats, scissors, chairs, faces, shoes and scrambled control images, examples in Fig. 10). Each subject participated 12 sessions of experiment. In each session, the subjects viewed images of eight object categories, with 9 full-brain measurements per category.

We assessed performance by training linear classifiers to discriminate between pairs of objects, e.g., face vs. bottle, for each of the 28 possible binary classifications among 8 objects. We trained the weights \mathbf{w} for each model using linear regression from fMRI measurements \mathbf{x} to binary labels $y \in \{-1, +1\}$, and assessed accuracy on the test set using predicted labels $\hat{y} = \text{sign}(\mathbf{w}^\top \mathbf{x})$. We divided 12 sessions of data per subject into train-test splits of 5:7, 6:6



Figure 10: Examples of the stimuli for 7 categories (except for scrambled control images).

and 7:5. When training with data from N sessions, the training dataset consisted of $18N$ full-brain measurements (9 measurements per category $\times 2$ categories). Each measurement contained $24,083$ valid voxels from a $40 \times 64 \times 64$ 3D volume.

Fig. 11 shows the classification performance of lasso, GraphNet, TV-L1, DRD, and smooth-DRD estimators, averaged over 6 subjects and across the three train-test splits. The smooth-DRD estimate achieved the highest accuracy for most of the binary classifications, while the DRD estimate achieved second highest accuracy. The left column in Fig. 12 shows the regression weights estimated for the house vs. bottle classification task. The DRD and smooth-DRD weights both had significant positive regions in the parahippocampal place area (PPA), an area known to respond to images of places (Epstein et al., 1999) and negative regions in the lateral occipital complex (LOC), an area known to respond to objects (Eger et al., 2008). By comparison, TV-L1 and GraphNet weights in LOC were neither strong nor clustered. The right column in Fig. 12 shows regression weights for the face vs. scrambled-pixels classification task. All methods managed to discover active responses around LOC and fusiform face area (FFA) (specialized for facial recognition) (Kanwisher et al., 1997), though DRD and smooth-DRD weights exhibited fewer isolated non-zero weights in areas far from the temporal and occipital lobes.

8. Discussion

In this paper, we introduced dependent relevance determination (DRD), a hierarchical Bayesian model for sparse, localized, and smooth regression weights. This model is appropriate for regression settings in which the regressors can be arranged geometrically as a vector, matrix, or tensor, with local dependencies that depend on distance within this structure (e.g., tensors of 3D brain measurements).

The DRD model takes its inspiration from the automatic relevance determination (ARD) model (Tipping, 2001), but adds a Gaussian process to introduce dependencies between prior variances of regression weights as a function of distance between their regressors. Samples

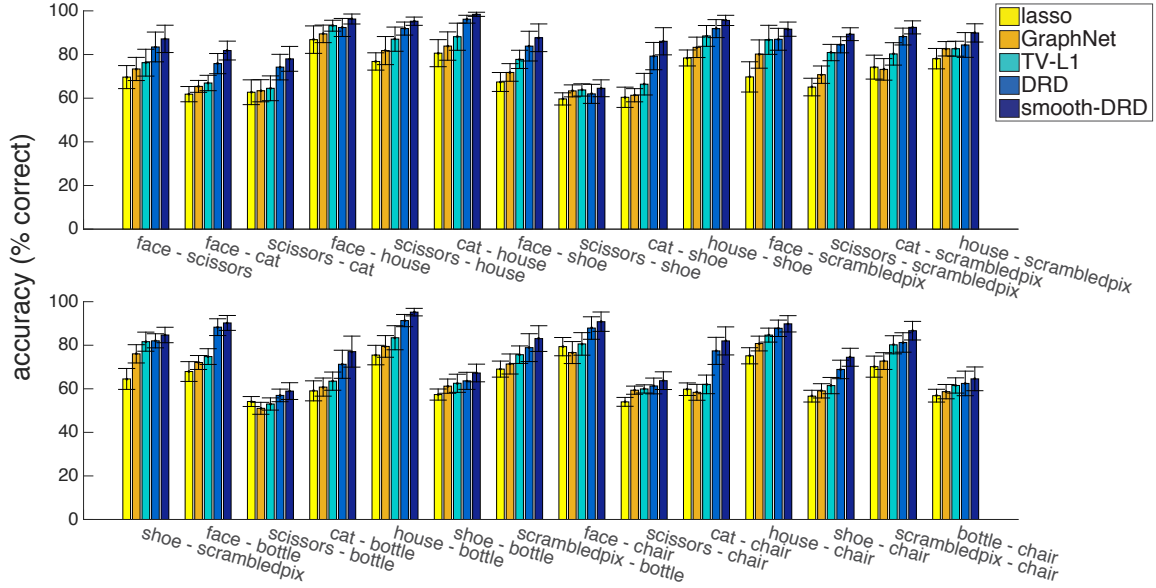


Figure 11: Classification accuracy performance for lasso, GraphNet, TV-L1, DRD and smooth-DRD, averaged across 6 subjects and three different train-test splits (5:7, 6:6 and 7:5). Error bars indicate ± 1 standard error of the mean, averaged over train-test splits. The x-axis labels indicate pairs of object categories considered for binary classification.

from the DRD prior therefore exhibit clustering of non-zero weights. However, weights sampled from the standard DRD prior are uncorrelated, meaning there is no tendency for such weight tensors to be smooth. For this reason, we introduced the smooth-DRD model, which composes the standard DRD prior with a smoothness-inducing covariance function (Sahani and Linden, 2003; Park and Pillow, 2011). Weights sampled from the resulting model tend to be sparse as well as smooth, with islands of smooth, non-zero weight features surrounded by oceans of zeros.

We described two methods for inferring the model parameters: one based on the Laplace approximation and a second based on MCMC. We proposed a novel variant of the Laplace based approach involving a two-stage convex relaxation of the log posterior. We examined phase transitions between perfect and imperfect recovery, showing that the DRD and smooth-DRD model can achieve perfect recovery with far fewer measurements when the non-zero weights in a signal are clustered or clustered and smooth.

Lastly, we carried out experiments to compare DRD with a variety of other methods, including lasso, GraphNet, and TV-L1. We found that, for several different brain imaging datasets, DRD achieved better prediction performance than previous methods, while also achieving high interpretability with regression/classification weights defined by smooth, clustered sets of voxels.

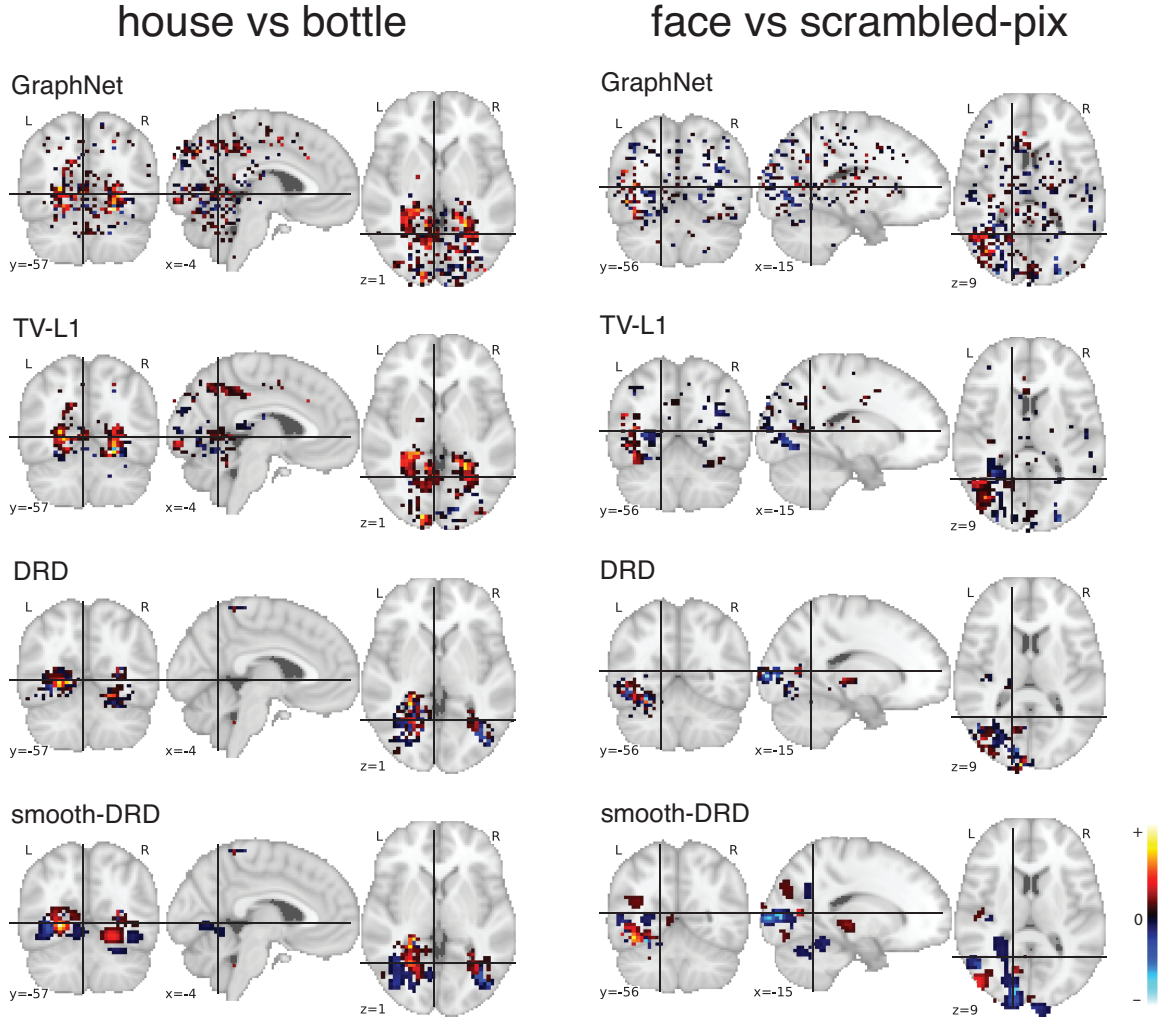


Figure 12: **Left column:** weight maps for the house vs bottle pair. **Right column:** weight maps for the face vs scrambled-pix pair. The methods shown are GraphNet, TV-L1, DRD and smooth-DRD.

The DRD and smooth-DRD models offer a powerful statistical framework for attacking problems in which sparsity is overlaid with local dependencies, a scenario that arises commonly in (for example) spatial and temporal regression problems. Recent work has shown successful application of a closely related model for capturing dependencies between sparse variables in genomic data (Engelhardt and Adams, 2014). In future work, we expect the DRD modeling framework to find applications beyond the regression setting, including structured latent factor models (Chen et al., 2015) and false discovery rate estimation (Tansey et al., 2017).

Acknowledgments

This work was supported by grants from the Sloan Foundation (JWP), McKnight Foundation (JWP), Simons Collaboration on the Global Brain (SCGB AWD1004351, JWP), and the NSF CAREER Award (IIS-1150186, JWP).

References

- Dennis Amelunxen, Martin Lotz, Michael B McCoy, and Joel A Tropp. Living on the edge: Phase transitions in convex programs with random data. *Information and Inference*, page iau005, 2014.
- Michael R Andersen, Ole Winther, and Lars K Hansen. Bayesian inference for structured spike and slab priors. In *Advances in Neural Information Processing Systems*, pages 1745–1753, 2014.
- Michael Riis Andersen, Aki Vehtari, Ole Winther, and Lars Kai Hansen. Bayesian inference for spatio-temporal spike and slab priors. *arXiv preprint arXiv:1509.04752*, 2015.
- Luca Baldassarre, Janaina Mourao-Miranda, and Massimiliano Pontil. Structured sparsity models for brain decoding from fmri data. In *Pattern Recognition in NeuroImaging (PRNI), 2012 International Workshop on*, pages 5–8. IEEE, 2012.
- Stephen Boyd and Lieven Vandenberghe. *Convex optimization*. Cambridge university press, 2004.
- Melissa K Carroll, Guillermo A Cecchi, Irina Rish, Rahul Garg, and A Ravishankar Rao. Prediction and interpretation of distributed neural activity with sparse models. *NeuroImage*, 44(1):112–122, 2009.
- Carlos M Carvalho, Nicholas G Polson, and James G Scott. Handling sparsity via the horseshoe. In *International Conference on Artificial Intelligence and Statistics*, pages 73–80, 2009.
- Po-Hsuan Cameron Chen, Janice Chen, Yaara Yeshurun, Uri Hasson, James Haxby, and Peter J Ramadge. A reduced-dimension fmri shared response model. In *Advances in Neural Information Processing Systems*, pages 460–468, 2015.
- Hanna Cho, Jeong-Hun Kim, Changsoo Kim, Byoung Seok Ye, Hee Jin Kim, Cindy W Yoon, Young Noh, Geon Ha Kim, Yeo Jin Kim, Jung-Hyun Kim, et al. Shape changes of the basal ganglia and thalamus in alzheimer’s disease: a three-year longitudinal study. *Journal of Alzheimer’s Disease*, 40(2):285–295, 2014.
- LW De Jong, K Van der Hiele, IM Veer, JJ Houwing, RGJ Westendorp, ELEM Bollen, PW De Bruin, HAM Middelkoop, MA Van Buchem, and J Van Der Grond. Strongly reduced volumes of putamen and thalamus in alzheimer’s disease: an mri study. *Brain*, 131(12):3277–3285, 2008.

- Evelyn Eger, John Ashburner, John-Dylan Haynes, Raymond J Dolan, and Geraint Rees. fmri activity patterns in human loc carry information about object exemplars within category. *Journal of cognitive neuroscience*, 20(2):356–370, 2008.
- Barbara E Engelhardt and Ryan P Adams. Bayesian structured sparsity from gaussian fields. *arXiv preprint arXiv:1407.2235*, 2014.
- Russell Epstein, Alison Harris, Damian Stanley, and Nancy Kanwisher. The parahippocampal place area: Recognition, navigation, or encoding? *Neuron*, 23(1):115–125, 1999.
- Jerome Friedman, Trevor Hastie, and Robert Tibshirani. A note on the group lasso and a sparse group lasso. *arXiv preprint arXiv:1001.0736*, 2010.
- Surya Ganguli and Haim Sompolinsky. Statistical mechanics of compressed sensing. *Physical review letters*, 104(18):188701, 2010.
- Marcel V Gerven, Botond Cseke, Robert Oostenveld, and Tom Heskes. Bayesian source localization with the multivariate laplace prior. In *Advances in Neural Information Processing Systems*, pages 1901–1909, 2009.
- Alexandre Gramfort, Bertrand Thirion, and Gaël Varoquaux. Identifying predictive regions from fmri with tv-l1 prior. In *Pattern Recognition in Neuroimaging (PRNI), 2013 International Workshop on*, pages 17–20. IEEE, 2013.
- L Grosenick, B Klingenberg, B Knutson, and JE Taylor. A family of interpretable multivariate models for regression and classification of whole-brain fmri data. *arXiv preprint arXiv:1110.4139*, 2011.
- Asela Gunawardana and William Byrne. Convergence theorems for generalized alternating minimization procedures. *Journal of machine learning research*, 6(Dec):2049–2073, 2005.
- James V Haxby, M Ida Gobbini, Maura L Furey, Alumit Ishai, Jennifer L Schouten, and Pietro Pietrini. Distributed and overlapping representations of faces and objects in ventral temporal cortex. *Science*, 293(5539):2425–2430, 2001.
- Daniel Hernández-Lobato and José Miguel Hernández-Lobato. Learning feature selection dependencies in multi-task learning. In *Advances in Neural Information Processing Systems*, pages 746–754, 2013.
- Daniel Hernández-Lobato, José Miguel Hernández-Lobato, and Pierre Dupont. Generalized spike-and-slab priors for bayesian group feature selection using expectation propagation. *The Journal of Machine Learning Research*, 14(1):1891–1945, 2013.
- Nicholas J Higham. *Accuracy and stability of numerical algorithms*. SIAM, 2002.
- Junzhou Huang, Tong Zhang, and Dimitris Metaxas. Learning with structured sparsity. *The Journal of Machine Learning Research*, 12:3371–3412, 2011.
- Laurent Jacob, Guillaume Obozinski, and Jean-Philippe Vert. Group lasso with overlap and graph lasso. In *Proceedings of the 26th Annual International Conference on Machine Learning*, pages 433–440. ACM, 2009.

- Rodolphe Jenatton, Jean-Yves Audibert, and Francis Bach. Structured variable selection with sparsity-inducing norms. *The Journal of Machine Learning Research*, 12:2777–2824, 2011.
- Nancy Kanwisher, Josh McDermott, and Marvin M Chun. The fusiform face area: a module in human extrastriate cortex specialized for face perception. *The Journal of Neuroscience*, 17(11):4302–4311, 1997.
- Seyoung Kim and Eric P Xing. Statistical estimation of correlated genome associations to a quantitative trait network. *PLoS genetics*, 5(8):e1000587, 2009.
- Miguel Lázaro-Gredilla, Joaquin Quiñonero-Candela, Carl Edward Rasmussen, and Aníbal R Figueiras-Vidal. Sparse spectrum gaussian process regression. *The Journal of Machine Learning Research*, 11:1865–1881, 2010. URL <http://www.jmlr.org/papers/v11/lazaro-gredilla10a.html>.
- Han Liu, Larry Wasserman, and John D Lafferty. Nonparametric regression and classification with joint sparsity constraints. In *Advances in neural information processing systems*, pages 969–976, 2009.
- David JC MacKay. Bayesian interpolation. *Neural computation*, 4(3):415–447, 1992.
- David JC MacKay. *Information theory, inference and learning algorithms*. Cambridge university press, 2003.
- Daniel S Marcus, Tracy H Wang, Jamie Parker, John G Csernansky, John C Morris, and Randy L Buckner. Open access series of imaging studies (oasis): cross-sectional mri data in young, middle aged, nondemented, and demented older adults. *Journal of cognitive neuroscience*, 19(9):1498–1507, 2007.
- Vincent Michel, Alexandre Gramfort, Gaël Varoquaux, Evelyn Eger, and Bertrand Thirion. Total variation regularization for fmri-based prediction of behavior. *Medical Imaging, IEEE Transactions on*, 30(7):1328–1340, 2011.
- Toby J Mitchell and John J Beauchamp. Bayesian variable selection in linear regression. *Journal of the American Statistical Association*, 83(404):1023–1032, 1988.
- Iain Murray and Ryan P Adams. Slice sampling covariance hyperparameters of latent gaussian models. In *Advances in Neural Information Processing Systems*, pages 1732–1740, 2010.
- Iain Murray, Ryan Prescott Adams, and David JC MacKay. Elliptical slice sampling. *arXiv preprint arXiv:1001.0175*, 2009.
- Radford M Neal. *Bayesian learning for neural networks*. PhD thesis, University of Toronto, 1995.
- Mijung Park and Jonathan W Pillow. Receptive field inference with localized priors. *PLoS computational biology*, 7(10):e1002219, 2011.

- Trevor Park and George Casella. The bayesian lasso. *Journal of the American Statistical Association*, 103(482):681–686, 2008.
- Maneesh Sahani and Jennifer F Linden. Evidence optimization techniques for estimating stimulus-response functions. *Advances in neural information processing systems*, pages 317–324, 2003.
- Alexander Schmolck. *Smooth Relevance Vector Machines*. PhD thesis, University of Exeter, 2008.
- Michael L Stein. *Interpolation of Spatial Data: Some Theory for Kriging*. Springer, 1999.
- Wesley Tansey, Oluwasanmi Koyejo, Russell A. Poldrack, and James G. Scott. False discovery rate smoothing. *Journal of the American Statistical Association*, 0(ja):0–0, 2017. doi: 10.1080/01621459.2017.1319838. URL <http://dx.doi.org/10.1080/01621459.2017.1319838>.
- Robert Tibshirani. Regression shrinkage and selection via the lasso. *Journal of the Royal Statistical Society. Series B (Methodological)*, pages 267–288, 1996.
- ACFME Tipping and AC Faul. Analysis of sparse bayesian learning. *Advances in neural information processing systems*, 14:383–389, 2002.
- M. E. Tipping and A. C. Faul. Fast marginal likelihood maximisation for sparse bayesian models. In C. M. Bishop and B. J. Frey, editors, *Proceedings of the ninth international workshop on artificial intelligence and statistics*, volume 1(3), pages 1–13. Citeseer, 2003.
- Michael E Tipping. Sparse bayesian learning and the relevance vector machine. *The journal of machine learning research*, 1:211–244, 2001.
- Sabrina M Tom, Craig R Fox, Christopher Trepel, and Russell A Poldrack. The neural basis of loss aversion in decision-making under risk. *Science*, 315(5811):515–518, 2007.
- Sabrina M Tom, Craig R Fox, Christopher Trepel, and Russell A Poldrack. Mixed-gambles task, 2011. This data was obtained from the OpenfMRI database. Its accession number is ds000005, <http://https://openfmri.org/dataset/ds000005/>.
- David Wipf and Srikantan Nagarajan. A new view of automatic relevance determination. In J.C. Platt, D. Koller, Y. Singer, and S. Roweis, editors, *Advances in Neural Information Processing Systems 20*, pages 1625–1632. MIT Press, Cambridge, MA, 2008.
- Lei Yu, Hong Sun, Jean-Pierre Barbot, and Gang Zheng. Bayesian compressive sensing for cluster structured sparse signals. *Signal Processing*, 92(1):259–269, 2012.
- Ming Yuan and Yi Lin. Model selection and estimation in regression with grouped variables. *Journal of the Royal Statistical Society: Series B (Statistical Methodology)*, 68(1):49–67, 2006.
- Willard I Zangwill. *Nonlinear programming: a unified approach*. Prentice-Hall, 1969.

Appendix A. The Hessian of the negative log-posterior in Laplace approximation for smooth-DRD

Now we derive the Hessian matrix inside of the inverse of (eq. 22).

$$H = -\frac{\partial^2}{\partial \mathbf{u} \partial \mathbf{u}^\top} \left[\log p(\mathbf{y} | X, \mathbf{u}, \sigma^2, \delta) + \log p(\mathbf{u} | \boldsymbol{\theta}_{drd}) \right]. \quad (52)$$

The first term to take the partial derivatives of is (eq. 20):

$$\log p(\mathbf{y} | X, \mathbf{u}, \sigma^2, \delta) = -\frac{1}{2} \log |XCX^\top + \sigma^2 I| - \frac{1}{2} \mathbf{y}^\top (XCX^\top + \sigma^2 I)^{-1} \mathbf{y} + \text{const} \quad (53)$$

and the second is (eq. 21):

$$\log p(\mathbf{u} | \boldsymbol{\theta}_{drd}) = -\frac{1}{2} (\mathbf{u} - b\mathbf{1})^\top K^{-1} (\mathbf{u} - b\mathbf{1}) - \frac{1}{2} \log |K| + \text{const}. \quad (54)$$

Define $S = XCX^\top + \sigma^2 I$, where $C = C_{drd}^{\frac{1}{2}} \Sigma C_{drd}^{\frac{1}{2}}$. Let $Z = XC_{drd}^{\frac{1}{2}} \Sigma^{\frac{1}{2}}$, then,

$$S = XC_{drd}^{\frac{1}{2}} \Sigma C_{drd}^{\frac{1}{2}} X^\top + \sigma^2 I = ZZ^\top + \sigma^2 I \quad (55)$$

$$\log p(\mathbf{u} | \mathbf{y}, X, \boldsymbol{\theta}) = -\frac{1}{2} \mathbf{y}^\top S^{-1} \mathbf{y} - \frac{1}{2} \log |S| - \frac{1}{2} (\mathbf{u} - b\mathbf{1})^\top K^{-1} (\mathbf{u} - b\mathbf{1}) + \text{const}. \quad (56)$$

The first derivative with respect to \mathbf{u}_i is given by:

$$\frac{\partial}{\partial \mathbf{u}_i} \log p(\mathbf{u} | \mathbf{y}, X, \boldsymbol{\theta}) = \frac{1}{2} \frac{\partial}{\partial \mathbf{u}_i} \left(-\mathbf{y}^\top S^{-1} \mathbf{y} - \log |S| - (\mathbf{u} - b\mathbf{1})^\top K^{-1} (\mathbf{u} - b\mathbf{1}) \right) \quad (57)$$

$$= \frac{1}{\sigma^2} \text{Tr} \left[Z^\top S^{-1} \mathbf{y} \mathbf{y}^\top S^{-1} \left(\frac{\partial}{\partial \mathbf{u}_i} Z \right) - Z^\top S^{-1} \left(\frac{\partial}{\partial \mathbf{u}_i} Z \right) \right] \quad (58)$$

$$- [K^{-1} (\mathbf{u} - b\mathbf{1})]_i, \quad (59)$$

where

$$\frac{\partial}{\partial \mathbf{u}_i} Z = X \left(\frac{\partial}{\partial \mathbf{u}_i} C_{drd}^{\frac{1}{2}} \right) \Sigma^{\frac{1}{2}}. \quad (60)$$

The second derivative with respect to \mathbf{u}_j is given by:

$$\frac{\partial^2}{\partial \mathbf{u}_i \partial \mathbf{u}_j} \log p(\mathbf{u} | \mathbf{y}, X, \boldsymbol{\theta}) = H_1 + H_2 + H_3 - K_{ij}^{-1} = -H_{ij}, \quad (61)$$

$$H_1 = \frac{1}{\sigma^2} \text{Tr} \left[Z^\top S^{-1} \mathbf{y} \mathbf{y}^\top S^{-1} \left(\frac{\partial^2}{\partial \mathbf{u}_i \partial \mathbf{u}_j} Z \right) - Z^\top S^{-1} \left(\frac{\partial^2}{\partial \mathbf{u}_i \partial \mathbf{u}_j} Z \right) \right], \quad (62)$$

$$H_2 = \frac{1}{\sigma^2} \text{Tr} \left[\left(\frac{\partial}{\partial \mathbf{u}_j} Z \right)^\top S^{-1} \mathbf{y} \mathbf{y}^\top S^{-1} \left(\frac{\partial}{\partial \mathbf{u}_i} Z \right) - \left(\frac{\partial}{\partial \mathbf{u}_j} Z \right)^\top S^{-1} \left(\frac{\partial}{\partial \mathbf{u}_i} Z \right) \right], \quad (63)$$

$$H_3 = \frac{2}{\sigma^2} \text{Tr} \left[-Z^\top S^{-1} Z^\top \left(\frac{\partial}{\partial \mathbf{u}_j} Z \right) S^{-1} \mathbf{y} \mathbf{y}^\top S^{-1} \left(\frac{\partial}{\partial \mathbf{u}_i} Z \right) \right] \quad (64)$$

$$-Z^\top S^{-1} \mathbf{y} \mathbf{y}^\top S^{-1} Z^\top \left(\frac{\partial}{\partial \mathbf{u}_j} Z \right) S^{-1} \left(\frac{\partial}{\partial \mathbf{u}_i} Z \right) \quad (65)$$

$$+Z^\top S^{-1} Z^\top \left(\frac{\partial}{\partial \mathbf{u}_j} Z \right) S^{-1} \left(\frac{\partial}{\partial \mathbf{u}_i} Z \right) \Big], \quad (66)$$

where

$$\frac{\partial^2}{\partial \mathbf{u}_i \partial \mathbf{u}_j} Z = X \left(\frac{\partial^2}{\partial \mathbf{u}_i \partial \mathbf{u}_j} C_{drd}^{\frac{1}{2}} \right) \Sigma^{\frac{1}{2}}. \quad (67)$$

For DRD only, we can just derive the Hessian by replacing $C_{drd}^{\frac{1}{2}} \Sigma^{\frac{1}{2}}$ with $C_{drd}^{\frac{1}{2}}$.

Appendix B. Proof of convexity of $\mathcal{L}_1(\mathbf{u})$

We ignore the scaling $\frac{1}{2}$ here for simplicity, and write,

$$\mathcal{L}_1(\mathbf{u}) = \log |X \text{diag}(e^{\mathbf{u}}) X^\top + \sigma^2 I| \quad (68)$$

$$= \log \left| \text{diag}(e^{\mathbf{u}}) \frac{X^\top X}{\sigma^2} + I \right| + \text{const} \quad (69)$$

$$= \log \left| \frac{X^\top X}{\sigma^2} + \text{diag}(e^{-\mathbf{u}}) \right| + \log |\text{diag}(e^{\mathbf{u}})| + \text{const}. \quad (70)$$

Let $V = \frac{X^\top X}{\sigma^2}$, which is p.s.d., then

$$\begin{aligned} \frac{\partial}{\partial \mathbf{u}} \log |V + \text{diag}(e^{-\mathbf{u}})| &= -\text{diag} \left((\text{diag}(e^{-\mathbf{u}}) + V)^{-1} \odot \text{diag}(e^{-\mathbf{u}}) \right) \\ \frac{\partial^2}{\partial^2 \mathbf{u}} \log |V + \text{diag}(e^{-\mathbf{u}})| &= (V(\text{diag}(e^{\mathbf{u}})V + I)^{-1}) \odot (\text{diag}(e^{-\mathbf{u}}) + V)^{-1}, \end{aligned} \quad (71)$$

where \odot is the Hadamard product. Moreover, we know that

$$\begin{aligned} V(\text{diag}(e^{\mathbf{u}})V + I)^{-1} &= \frac{X^\top X}{\sigma^2} (\text{diag}(e^{\mathbf{u}}) \frac{X^\top X}{\sigma^2} + I)^{-1} \\ &= X^\top (X \text{diag}(e^{\mathbf{u}}) X^\top + \sigma^2 I)^{-1} X \succeq 0. \end{aligned} \quad (72)$$

Thanks to the Schur product theorem stating that the Hadamard product of two positive definite matrices is also a positive definite matrix, we have $\frac{\partial^2}{\partial^2 \mathbf{u}} \log |V + \text{diag}(e^{-\mathbf{u}})| \succeq 0$, thus $\log \left| \frac{X^\top X}{\sigma^2} + \text{diag}(e^{-\mathbf{u}}) \right|$ is convex in \mathbf{u} . In addition, $\log |\text{diag}(e^{\mathbf{u}})|$ is also convex in \mathbf{u} . Therefore, $\mathcal{L}_1(\mathbf{u})$ is convex in \mathbf{u} .

Appendix C. Proof of boundness and nonemptiness of $\mathcal{F}(\mathbf{u})$

We want to prove that for eq. 35, when $\|\mathbf{u}\| \rightarrow \infty$, we have $\mathcal{F}(\mathbf{u}) \rightarrow \infty$. Rewrite \mathcal{F} here,

$$\mathcal{F}(\mathbf{u}) = \mathbf{z}^{k^\top} \mathbf{h}(\mathbf{u}) - \mathcal{L}_{\mathbf{h}}^*(\mathbf{z}) + \mathcal{L}_1(\mathbf{u}) + \mathcal{L}_3(\mathbf{u}) \quad (73)$$

where $\mathbf{h}(\mathbf{u}) = e^{-\mathbf{u}}$, $\mathcal{L}_1(\mathbf{u}) = \frac{1}{2} \log |X \text{diag}(e^{\mathbf{u}}) X^\top + \sigma^2 I|$ and $\mathcal{L}_3(\mathbf{u}) = \frac{1}{2} (\mathbf{u} - b\mathbf{1})^\top K^{-1} (\mathbf{u} - b\mathbf{1})$.

1) Each element in $\mathbf{h}(\mathbf{u})$ is bounded by 0 and 1. Thus when $\|\mathbf{u}\| \rightarrow \infty$, $\mathbf{z}^k{}^\top \mathbf{h}(\mathbf{u})$ will be bounded.

2) K^{-1} is a positive semidefinite (psd) matrix. Thus $\mathcal{L}_3(\mathbf{u})$ is lower-bounded by 0. When $\|\mathbf{u}\| \rightarrow \infty$, $\mathcal{L}_3(\mathbf{u}) \geq 0$. The upper bound is unclear.

3) Denote $\Gamma = \text{diag}(e^{\mathbf{u}})$ whose diagonal values are all nonnegative. Now we want to prove when $\|\mathbf{u}\| \rightarrow \infty$, we have $\mathcal{L}_1(\mathbf{u}) = \frac{1}{2} \log |X \Gamma X^\top + \sigma^2 I| \rightarrow \infty$.

First, we note that $\mathcal{L}_1(\mathbf{u})$ has a lower bound. It can be easily shown that the eigenvalues of $X \Gamma X^\top + \sigma^2 I$ should be greater than or equal to σ^2 , given $X \Gamma X^\top$ is a psd matrix.

If $\|\mathbf{u}\| \rightarrow \infty$, we can assume $u_1 \rightarrow \infty, \dots, u_s \rightarrow \infty$ where $\mathbf{u} \in \mathbb{R}^p$ and $s \leq p$, then $e^{u_i} \rightarrow \infty$, for all $i = \{1, \dots, s\}$. For $\{u_i\}_{i=s+1}^p$, if u_i is finite, e^{u_i} will be finite; else if $u_i \rightarrow -\infty$, $e^{u_i} = 0$. Thus e^{u_i} is a finite value for all $i = \{s+1, \dots, p\}$. We can write Γ as an addition of two matrices A and B , i.e. $\Gamma = A + B$.

$$A = \begin{bmatrix} e^{u_1} & & & & \\ & e^{u_2} & & & \\ & & \ddots & & \\ & & & e^{u_s} & \\ & & & & 0 \\ & 0 & & & & \ddots \\ & & & & & & 0 \end{bmatrix}, \quad B = \begin{bmatrix} 0 & & & & \\ & 0 & & & \\ & & \ddots & & \\ & & & 0 & \\ & & & & e^{u_{s+1}} \\ 0 & & & & & \ddots \\ & & & & & & e^{u_p} \end{bmatrix} \quad (74)$$

The nonzero elements in A are infinite values. The nonzero elements in B are finite non-negative values. Let $M = X B X^\top + \sigma^2 I \in \mathbb{R}^{n \times n}$. $X B X^\top$ is a psd matrix. The smallest eigenvalue of $X B X^\top$ should be nonnegative. Therefore the smallest eigenvalue of M is greater than or equal to σ^2 . This implies the invertibility of M . Since M^{-1} is also positive definite, we can factorize M^{-1} into $S \in \mathbb{R}^{n \times n}$ and S^\top , i.e. $M^{-1} = S S^\top$. Thus, we can write

$$\mathcal{L}_1(\mathbf{u}) = \frac{1}{2} \log |X A X^\top + X B X^\top + \sigma^2 I| \quad (75)$$

$$= \frac{1}{2} \log |X A X^\top + M| \quad (76)$$

$$= \frac{1}{2} \log |X A X^\top M^{-1} + I| + \frac{1}{2} \log |M| \quad (77)$$

$$= \frac{1}{2} \log |X A X^\top S S^\top + I| + \frac{1}{2} \log |M| \quad (78)$$

$$= \frac{1}{2} \log |S^\top X A X^\top S + I| + \frac{1}{2} \log |M| \quad (79)$$

Combining $X^\top S$ to be one matrix $Z \in \mathbb{R}^{p \times n}$, we can investigate the elements in $Z^\top A Z$. $Z^\top A Z$ should be equal to $\infty * \tilde{Z}^\top \tilde{Z}$ where $\tilde{Z} \in \mathbb{R}^{s \times n}$ is a trimmed Z by throwing away the rows with indices from $s+1$ to p . Therefore, nonzero eigenvalues of $\tilde{Z}^\top \tilde{Z}$ will turn into ∞ in $Z^\top A Z$. Zero eigenvalues will remain zero.

Let $\lambda_i \geq 0$ denote the i th eigenvalue of $Z^\top AZ$, then

$$\mathcal{L}_1(\mathbf{u}) = \frac{1}{2} \sum_{i=1}^p \log(\lambda_i + 1) + \frac{1}{2} \log |M| \quad (80)$$

Since there exists at least one eigenvalue λ_i in $Z^\top AZ$ approaching to ∞ , we can conclude that $\mathcal{L}_1(\mathbf{u})$ also approaches to ∞ in such a case.

Accordingly, if $\|\mathbf{u}\| \rightarrow \infty$, we have $\mathcal{F}(\mathbf{u}) \rightarrow \infty$, then there must exist a solution set for minimizing $\mathcal{F}(\mathbf{u})$. This validates the nonemptiness of the solution set. Furthermore, the solution set must be bounded. If it's not bounded, there must be a solution at ∞ with the minimal $\mathcal{F}(\mathbf{u})$, but this contradicts the assumption that $\mathcal{F}(\mathbf{u}) \rightarrow \infty$ when $\|\mathbf{u}\| \rightarrow \infty$. Therefore, we can claim that the solution set of $\mathcal{F}(\mathbf{u})$ is bounded and nonempty.